Macromolecules

pubs.acs.org/Macromolecules Article

Entropy-Induced Localization and Sliding Dynamics of Rings on Polyrotaxane

Yan Wang, Hui Lu, Xiang-Meng Jia, An-Chang Shi,* Jiajia Zhou,* Guojie Zhang,* and Hong Liu*

Cite This: *Macromolecules* 2024, 57, 1846−1858 Read Online

ACCESS | Metrics & More | Article Recommendations | Supporting Information

ABSTRACT: Regulating the position and sliding dynamics of rings on the polyrotaxane (PR) backbone plays a crucial role in determining the properties and/or functions of PR and PR-based soft materials. In this work, we use molecular dynamics simulations to reveal that the features of localization and sliding dynamics of rings on a PR modeled by a rod−coil−rod triblock copolymer are regulated by the entropy effect of the coil block. The distribution of the rings along the rod−coil−rod PR backbone is found to be highly heterogeneous and can be described by a two-state model characterized by a (free) energy gap, ΔE, which depends on the three characteristic parameters of the PR system, $\Delta E = \Delta E(\alpha, \mu, \rho_{ring})$, where α is the ratio of the rod to the coil strand length, μ is a quantity of measuring the stretching degree of the coil block, and ρ_{ring} is the overall ring coverage along the PR backbone. A theoretical model is proposed to describe the origin of this universality, the prediction of which is quantitatively consistent with simulation results for the single-ring rod−coil−rod PR system. The existence of an energy gap also gives a model for the dynamics of ring sliding along the PR backbone.

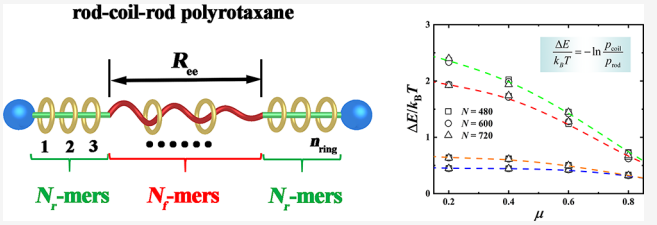

1. INTRODUCTION

Topological constraint is one of the most fundamental and important concepts in polymer physics, which plays a crucial role in determining the properties of polymers in many situations.[1−5] During the past decade, mechanically interlocked polymers (MIPs),[6−11] which are formed based on topological bonds, have been attracting much attention from polymer scientists, with polyrotaxane (PR)[7−10] and polycatenane[6,11] being two typical representatives. MIPs are common in nature; e.g., many protein catenanes[12−20] and DNA catenanes[21,22] have been found in living systems. Furthermore, MIPs have also been successfully synthesized in laboratory during the past decade.[23−33] The most distinguished features of MIPs lie in their unique modes of chain dynamics, including ring sliding, rotation, twisting, etc., which provide additional resources of conformational entropy and thus bring about many useful properties, such as thermodynamic stability,[34,35] mechanical adaptability,[36,37] dynamic stability,[38−40] and stretchability.[41,42] Consequently, MIPs serve as promising candidates for functional materials with potential applications in various technologies, including molecular switches, molecular machines,[43−47] drug delivery, and catalysis.[48−50]

As one important class of MIPs, PR is a topologically complex polymer made of a backbone chain threaded with ring molecules.[51] Previous studies have revealed that the location of the ring molecules on the backbone of PR is one of the key regulators for the ultimate function and properties of materials made of PR and PR derivatives.[45] Therefore, exploring and understanding principles governing the spatial arrangement of ring molecules along the PR backbone is key to the rational design of functional PR materials. One strategy to regulate ring location on the polymer is to use block copolymer as the PR backbone.[36,37,52−54] Localization of the rings could be induced by the selectivity of different blocks.[55] As an example, Ito and co-workers utilized a poly(ethylene oxide)-*b*-poly(propylene oxide)-*b*-poly(ethylene oxide) (PEO−PPO−PEO) triblock copolymer as the backbone to confine β-cyclodextrins (CDs) on the PPO block[56] and showed that the mechanical properties of the materials obtained from such system can be tuned by the positions of CD rings on the linear backbone. It is also observed that locational transition of the rings on the backbone chain could occur in PRs with block copolymers as their backbone.[57] In systems of the PR synthesized by Yui et al.,[58] the rings could be located at the ring-attractive block at low temperature and distributed randomly along the whole PR backbone chain at high temperature.[53] Introducing a coordination bond between the ring and the backbone of the PR[59−61] is another strategy for controlling the location of rings on the PR backbone. The rings will be located at certain positions along the backbone due to the coordination bonds, which prevent the dissociation of the rings from the PR. In addition, it is also possible to introduce bulky stoppers at

Received: September 6, 2023
Revised: January 24, 2024
Accepted: January 30, 2024
Published: February 12, 2024

https://doi.org/10.1021/acs.macromol.3c01805
Macromolecules 2024, 57, 1846−1858

different positions on the backbone, thus confining the rings within a certain range of the backbone.[62] Moreover, introducing covalent linkages between rotaxane backbone and ring molecules provides an alternative strategy to fix the rings on the PR.[63,64] We stress that the above-mentioned cases for controlling the ring location on PR all rely on regulating the interactions between the rings and the PR backbone.

In addition to the localization of rings, ring dynamics (e.g., sliding, hopping, etc.) along the PR backbone is also crucial for determining the physical properties of PR materials. For the PR and PR-based materials, it is the ring sliding along the PR backbone, due to the interlocked architecture of PR, that induces distinguishing properties. For instance, ring mobility has been revealed to act as a key regulator of structural formation and phase transitions of PR systems, such as melting, crystallization, etc., and thus of their mechanical properties.[11] Moreover, it is found that ring mobility in PR can also enhance the molecular recognition of ligand−receptor interactions, which is useful in many biological processes.[65,66] With PR as the precursor, slide-ring materials (SRMs) form a new kind of polymer network. Many studies of SRMs have revealed that the sliding dynamics of rings in PR also plays a crucial role in the mechanical property of SRMs.[36,67] For example, by using the α-CD threaded PR as the precursors, Okumura and Ito cross-linked the rings to prepare the typical SRMs[68] and concluded that the relative sliding motion between the cross-linked rings and the polymer backbone effectively reduced the Young's moduli and yielded the softness of the material. Furthermore, the mobility of cross-links in SRMs naturally eliminates the problem of stress concentration existing in covalently cross-linked networks and imbues them with an enhanced toughness.

Considering the central role of ring location and dynamics along PR backbones in determining the properties/functions of PR or PR derivatives,[69,70] a rational design of advanced PR-based soft materials will benefit from different strategies for controlling the ring positions and sliding dynamics on PR. In this study, we propose an entropy-based approach to the regulation of ring location and sliding dynamics along the PR with a rod−coil−rod triblock copolymer as the backbone. Notably, this model of rod−coil−rod polymer backbone could be realized experimentally by synthetic rod−coil−rod block copolymers, where the rod strands are either conjugated polymers[71] or aromatic rod molecules.[72] For instance, PRs (or polypseudorotaxanes) with conjugated backbones have been successfully formed from a polyfluorene-*alt*-biphenylene conjugated polymer threaded by β-cyclodextrin macrocycles,[73] and through the threading of cucurbit[n]urils (CB[n]) onto the positively charged poly(pyridyl vinylene).[74] In general, the localization and dynamics of the rings along the PR backbone should be determined by both the stiffness (i.e., rod−coil) of the polymer backbone and the interaction energy due to the chemical details of the polymer backbone and the threaded ring molecules. However, decoupling of these two different effects and thus understanding their own roles in affecting the location and dynamics of the rings along the PR backbone remain unreachable in experiments. On the other hand, this could be realized within the in silico study, where those above-mentioned effects could be simply decoupled through a suitable model construction. In this work, we aim to explore the role played by the chain stiffness of the PR backbone by purposely eliminating energetic differences between the molecular building blocks in controlling the ring location and dynamics along the PR backbone. We demonstrate that the rings prefer to be located at the rod block regions due to an entropic decrease of the coil block when they are located at the coil one. The feature of ring localization is well described by a two-state model characterized by a (free) energy gap. It is discovered that the energy difference is independent of the chain length of the backbone. Instead, it depends only on three characteristic parameters of the system. A theoretical model is proposed to understand this universality for a rod−coil−rod PR with a single ring. The existence of the energy gap also leads to a distinct feature of ring sliding along the PR backbone, i.e., hopping of rings from the rod block to the coil strand with the hopping time determined by the energy gap. This study provides a new method for controlling the location of threaded rings on PR and sheds light on understanding sliding dynamics of the rings in PR, and therefore, it could be useful for a rational design of PR or PR-based functional soft materials in experiments.

2. MODEL AND SIMULATION DETAILS

As depicted in Figure 1a, the PR system under study is composed of n_{ring} rings (yellow) threaded through a linear polymer backbone made of two rods (green lines) of N_r monomers and a coil (red line) strand with N_f monomers. Thus, $N = 2N_r + N_f$ denotes the total chain length of the backbone of PR. The two side rods in the backbone are blocked by two end-capping nanoparticles[75] (NPs, large blue beads) to prevent the escape of rings from the backbone. Each ring is composed of N_{ring} connected coarse-grained beads, whose rigidity is maintained by imposing a strong bending potential on the three adjacent bonded beads. Thus, the value of N_{ring} could also be used to reflect the inherent size of ring. In this study, we set $N_{ring} = 8$ for most of the cases. Notably, for simply studying the sliding of ring from the rod block to the coil strand, as well as its localization on the backbone in equilibrium, the positions of the rod blocks and two end-capping NPs are fixed during the simulation. In the initial configuration, n_{ring} individual rings are regularly arranged and threaded along the backbone polymer with suitable equivalent spacing. Once the simulation is started, all of the rings may slide along the PR following a Brownian motion. After a sufficiently long time, equilibrated distributions of rings on the polymer backbone can be achieved.

We employ the canonical ensemble coarse-grained MD simulations of the Kremer−Grest[76] model, which is a widely used generic model for studying conformational dynamics and rheological properties of polymers with topological constraints,[42] to describe motions of both the backbone polymer (more accurately, only the coil strand) and the rings on it. A truncated-shifted Lennard-Jones potential (also known as the Weeks−Chandler−Anderson, i.e., WCA potential[77]) is used to characterize the nonbonded interactions between any two coarse-grained beads in which the potential vanishes at the cutoff radius ($r_c = 2^{1/6}\sigma$) so that only repulsive part is left, i.e.,

$$U(r) = U_{LJ}(r) - U_{LJ}(r_c) \quad (1)$$

with

https://doi.org/10.1021/acs.macromol.3c01805
Macromolecules 2024, 57, 1846−1858

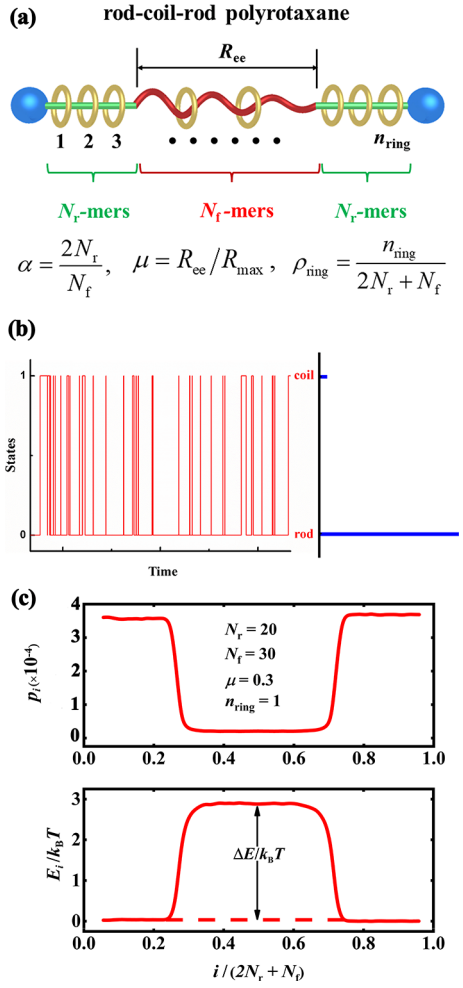

Figure 1. (a) Schematic illustration of the rod−coil−rod PR model and the three parameters μ, α, and ρ_{ring} characterizing its feature. Notably, the rod blocks (green) and end-capping NPs (blue) are all fixed during the simulation. (b) Time sequence of ring position on the rod block (State 0) or on the coil strand (State 1) for the single ring-threaded PR system (red plot). The probabilities (the blue columns) of the ring in these two states, P_{coil} and P_{rod}, are plotted. (c) The upper figure gives the probability distribution of a ring located at the i-th segment of the PR backbone, p_i, in the system with $N_r = 20$, $N_f = 30$, $\mu = 0.3$, $n_{ring} = 1$. Clearly, p_i remains constant for the ring staying at either the rod or the coil strand. The bottom figure shows the corresponding energy of the ring located at the i-th segment of the PR backbone, $E_i/k_BT = -\ln p_i + \text{const.}$ (note that the constant is chosen here such that $E_{rod}/k_BT = 0$). The result indicates that the two energy levels are degenerated essentially in which the degrees of degeneracy for states 0 and 1 are $2N_r$ and N_f, respectively, i.e., $P_{rod} \approx 2N_f p_{rod}$, $P_{coil} \approx N_f p_{coil}$, with p_{rod} and p_{coil} denoting the probabilities of the ring staying at any segment belonging to the rod and coil strands. Then, the energy gap between the two states of the ring can be obtained through them, i.e., $\Delta E/k_BT \equiv (E_{coil} - E_{rod})/k_BT = -\ln[p_{coil}/p_{rod}]$.

$$U_{LJ}(r) = \begin{cases} 4\varepsilon\left[\left(\frac{\sigma}{r - r_{EV}}\right)^{12} - \left(\frac{\sigma}{r - r_{EV}}\right)^{6}\right]; & (r \le r_c + r_{EV}) \\ 0 & (r > r_c + r_{EV}) \end{cases} \quad (2)$$

where ε is the potential well depth (i.e., the strength of interaction), σ is the length unit, and r_c is the cutoff radius which is set as $r_c = 2^{1/6}\sigma$. For simplicity, we define the units in the simulations by setting $\varepsilon = \sigma = m = 1.0$. The value r_{EV} is the size of the bead reflected by the volume exclusion between different interaction sites. Thus, for the interaction between the beads on the ring and those on the backbone polymer, we set $r_{EV} = r_b = 1.0\sigma$ with r_b representing the size of these common beads. As compared, for the end-capped NP in PR, for avoiding the rings to move out from the axial polymer, its size is set to obviously larger than 1.0σ, which should be comparable to the diameter of the ring. For example, for the ring composed of 8 coarse-grained beads ($N_{ring} = 8$), we can roughly evaluate its size as $D_0 = N_{ring} l_0/\pi = 2.4\sigma$. Here, $l_0 = 0.97\sigma$ is the mean value of bond length on the ring. Thus, the size of the NP is set as $d_{NP} = D_0$ to block the ring.

Bonded interactions between adjacent beads on the polymer backbone and the rings are characterized by a finitely extensible nonlinear elastic (FENE) spring potential[76]

$$U_{FENE} = -\frac{1}{2}kR_0^2 \ln\left(1 - \frac{r^2}{R_0^2}\right) \quad (3)$$

where $k = 30\varepsilon/\sigma^2$ and $R_0 = 1.5\sigma$ for all the bonds without the end-capped NPs. Under this set of parameters, the mean value of bond length could be kept as $l_0 = 0.97\sigma$ as aforementioned according to previous literature.[76] However, for the bond between the end-capped NP and the first bead on the axial polymer on both sides of the PR, for avoiding the crossing of bonds between this bond and those ones on the ring, and the further slipping out of the ring from the PR backbone, a different set of parameters should be utilized. Practically, we find $k = 30\varepsilon/\sigma^2$ and $R_0 = 2.2\sigma$ are safe enough to restrict its maximum stretching to make sure that the rings with size $N_{ring} = 8$ are not able to slip out from the polymer backbone.

To ensure a circle shape of the ring, the conventional harmonic bond angle potential[78,79] is imposed among the neighboring three beads in the ring to maintain the rigidity of the ring:

$$U_{angle} = \frac{1}{2}k_{bend}(\theta - \theta_0)^2 \quad (4)$$

where k_{bend} is the bending force constant set here as 350 ε and θ is the instantaneous angle between three connecting beads, and θ_0 is the equilibrium bond angle, which is set as 180° for all the bond angles in ring.

All simulations are performed by using the GALAMOST simulation package.[80] With the defined energy scale ε, the length scale σ and the bead mass m, the canonical ensemble MD simulations are performed with time step $dt = 0.005\sigma(m/\varepsilon)^{1/2}$ and temperature $T = \varepsilon/k_B$ with k_B as the Boltzmann constant. A short simulation of 5×10^5 time steps is first conducted to relax the system to eliminate the influence of the initial configuration. Following up is another simulation with at least 5×10^8 time steps to collect the data. All simulation data are obtained as the mean of 9−16 parallel samples by simultaneously generating these numbers of individual PRs regularly arranged in one simulation box, where a large distance between adjacent fixed PRs is set to avoid any possible interaction between them all through the simulation.

The model system can be characterized by three parameters, α, ρ_{ring}, and μ (see the definitions in Figure 1a). Here, $\alpha = 2N_r/N_f$ is the length ratio of rod block to the coil, $\rho_{ring} = n_{ring}/N$ is the ring coverage, or the number density of rings on PR backbone. Finally, the relative extension of the flexible coil strand is quantified by $\mu = R_{ee}/R_{max}$, where R_{ee} is root of mean-

https://doi.org/10.1021/acs.macromol.3c01805
Macromolecules 2024, 57, 1846−1858

squared end-to-end distance of the coil chain and R_{max} denotes its contour length, i.e., $R_{max} = N_f b$ with b representing the mean value of bond length in the Kremer–Grest[76] model.

3. RESULTS AND DISCUSSION

3.1. Heterogeneous Distribution of Rings along the PR Backbone. We first perform MD simulations of the rod–coil–rod PR with one ring to demonstrate its arrangement on the rod–coil–rod PR. The time evolution of the ring position for this simple PR system is shown in Figure 1b, from which the probability of ring location along the PR backbone can be extracted (shown in Figure 1b). The probability data clearly show that the ring prefers to locate on the rod blocks. Based on the ring location along the backbone, the current rod–coil–rod PR system could be regarded as a two-state system. Notably, the two-states model[81−84] has been successfully employed on explaining a wide range of physical phenomena at a basic level.[83,84] The key point is that there are two different states for the position of the ring, and the two states apparently have different (free) energy levels. At any specific time, the ring exclusively stays on either the rod strand or the coil one in which the two states have different energy levels. The ring switches dynamically between the two discrete states corresponding to its location. If we simply define the state of ring staying on the rod strand as 0, and that on the coil strand as 1, Figure 1b gives clear evidence that the current system is indeed a typical two-states system. Furthermore, our MD simulations reveal that the probability of finding the ring located at any segment of the coil and rod strand along the linear axis, which are denoted by p_{coil} and p_{rod}, remains constant (see data shown in Figure 1c), essentially indicating the two energy states are degenerated, and the degrees of degeneracy of the state 0 and 1 are $2N_r$ and N_f, respectively. In other words, the probabilities of the ring staying at the coil and the rod strands can be given by $P_{coil} \approx N_f p_{coil}$ and $P_{rod} \approx 2N_f p_{rod}$. Here, the (free) energy gap of the two states, $\Delta E/k_BT$, is defined as

$$\frac{\Delta E}{k_B T} \equiv \frac{E_{coil} - E_{rod}}{k_B T} = -\ln \frac{p_{coil}}{p_{rod}} \tag{5}$$

where k_B is the Boltzmann constant and T is the temperature.

We have carried out a large number of MD simulations for a wide range of system parameters (whose detailed information is given in the Supporting Information) to explore factors determining the energy gap between the two states. Our results revealed that the value of the energy gap, ΔE, is independent of the PR backbone chain length N. Rather, the energy gap is found to be a function of the three characteristic parameters of the system: the ratio of rod to coil length α, the relative extension of the coil strand $\mu = R_{ee}/R_{max}$, and the ring density ρ_{ring}, i.e., $\Delta E = \Delta E(\alpha, \mu, \rho_{ring})$. This conclusion is well supported by simulation results shown in Figure 2, which provides a collection of ΔE as a function of α, μ, and ρ_{ring} with different PR backbone chain length N (N = 480, 600, 720). As clearly shown in Figure 2, as long as these three parameters are the same, the dependence of ΔE on α, μ, or ρ_{ring} could perfectly collapse for systems with varying N. Notably, for the systems under study in this work, we find this quantitative dependence of ΔE on the three characteristic parameters is roughly valid in all of the parameter space considered. From the results shown in Figure 2 (especially Figure 2a,b), one can notice a quantitative trend of the energy gap of the two states

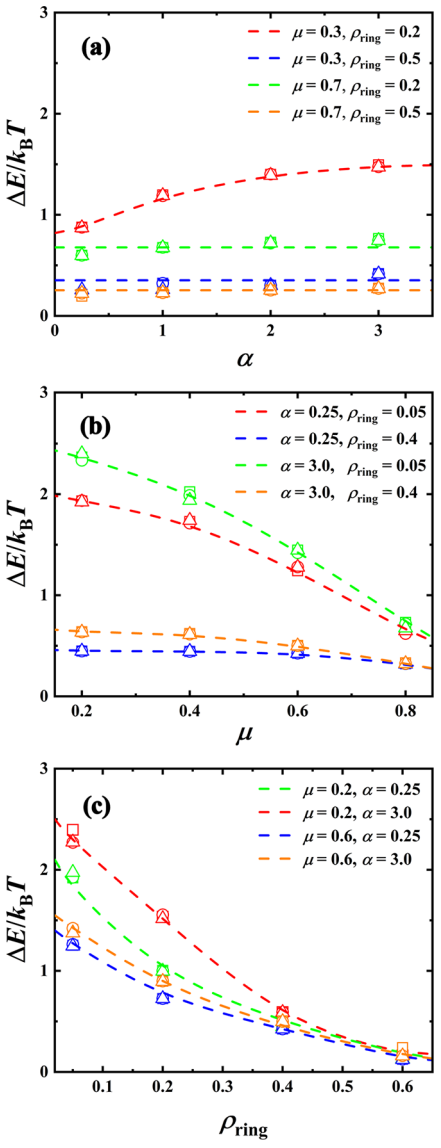

Figure 2. (a) The dependence of energy difference ΔE on the characteristic parameter α in the systems with N = 480, 600, and 720 while with different groups of μ and ρ_{ring}. (b) The dependence of ΔE on the characteristic parameter μ with N = 480, 600, and 720 while with different groups of α and ρ_{ring}. (c) The dependence of ΔE on the characteristic parameter ρ_{ring} in the systems with N = 480, 600, and 720 while with different groups of μ and α. The dashed lines in each subfigure are shown to guide the eye for each group. The different shapes of the symbols represent models with different chain lengths N. The squares correspond to N = 480, and the circles for N = 600 while the triangles for N = 720, respectively. Notably, the parameters of all systems as used in this figure are shown in Table S3 of the Supporting Information.

of rings $\Delta E/k_BT$ with respect to its three controlling parameters (α, μ, ρ_{ring}) that $\Delta E/k_BT$ becomes more and more independent of the value of the ratio of rod to coil length α, $\Delta E = \Delta E(\mu, \rho_{ring})$, when the coil chain of the PR backbone is more stretched, i.e., the relative extension of the coil strand μ gets increased.

To explore the molecular mechanism underlying the emergent (free) energy gap, ΔE, between the two states of the rings, we hypothesize that qualitatively the appearance of this free energy difference could be attributed to a decrease in

https://doi.org/10.1021/acs.macromol.3c01805
Macromolecules 2024, 57, 1846−1858

the conformational entropy of the coil strand (i.e., much-suppressed accessibility of the coil conformations) due to location of the rings at the coil strand, where additional excluded volume interactions (e.g., either between the coil segments and the ring segments or among the different rings located at the coil) get highly involved. We note that the excluded volume interaction underlies many interesting phenomena of the entropy-induced structural formation in soft matter, such as crystallization in densely packed hard spheres,[85] orientational ordering in concentrated liquid crystals,[86] and depletion in colloid−polymer systems,[87] etc. As de Gennes[2] pointed out, swelling behavior of a polymer chain conformation in good solvent, where effective excluded volume interactions between polymer segments are resulted, is also of entropic nature. Here, we design a series of simulations to test our hypothesis. As is well-known, in the case of polymer chains purely composed of hard-sphere segments, where the interaction energy always remains zero, it is the entropy that acts as the only physical origin of system behaviors. Therefore, if the value of ΔE is still positive in rod−coil−rod PR system composed of hard spheres, ΔE should be merely ascribed to the entropy contribution. To test this idea, we look into PR systems of the Kremer−Grest model with an increased value of the repulsive interaction parameter ε of WCA in eq 2, where the system approaches the hard sphere polymer model. As shown in Figure 3 with N = 480, it is apparent that for each

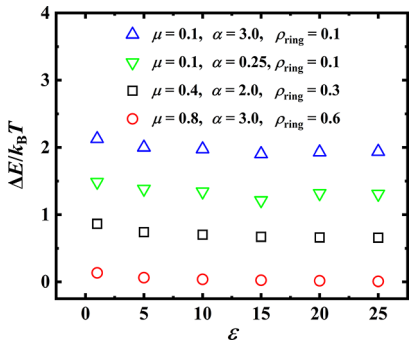

Figure 3. Dependence of energy difference $\Delta E/k_BT$ of the two states of the rings along the rod−coil−rod backbone on the repulsive interaction parameter ε in eq 2 in the systems with varying characteristic parameters α, μ, and ρ_{ring}. The chain length of the PR backbone in these systems is kept the same, N = 480.

system with the same characteristic parameters α, μ, and ρ_{ring}, $\Delta E/k_BT$ changes only slightly and ultimately approach a roughly converged value when the repulsive interaction parameter ε increases from 1 to as large as 25. Therefore, the above-mentioned entropy contribution (of the coil strand along the PR backbone) is indeed the dominant physical origin for the emerged ΔE.

We postulate that the emergence of energy gap $\Delta E/k_BT$ stems from an entropic loss of the coil strand when it is threaded by the rings. There could be two typical effects. First, the presence of a ring along the coil block would significantly deteriorate configurational accessibility of the segments spatially nearby due to the excluded volume interactions between the ring and the coil segments, which is termed as a locally entropic penalty of the coil segments. We note that this effect plays a role in any case of the system with varying characteristic parameters. Second, as the relative extension of the coil strand decreases, the excluded volume interactions between the segments within pervaded volume of the coil become more dominant. Therefore, there will be an increase of the excluded volume interactions when the coil chain is threaded by rings, which actually leads to an entropic loss of the coil conformation.

3.1.1. Locally Entropic Penalty of the Coil Segments. Here, we consider a simple rod−coil−rod PR system threaded with one single ring. Assume that the ring is located on the rod block, and there are $2N_r$ possible locations for the ring on the rod block. The partition function of the ring is then given by

$$\Omega_{rod} = 2N_r Z_0^{N_f} \tag{6}$$

where Z_0 is the partition function for one segment of the coil. Similarly, if the ring stays on the jointing point of two coil segments, the conformation of these two coil segments will be modified with the corresponding single-segmental partition function Z_1. The partition function of the system is now given by

$$\Omega_{coil} = N_f Z_1^2 Z_0^{N_f-2} \tag{7}$$

where N_f accounts for the number of possible positions for the ring along the coil strand. The entropy of the coil and rod blocks could be written as $S_{rod} = k_B \ln \Omega_{rod}$ and $S_{coil} = k_B \ln \Omega_{coil}$, respectively.

The origin of the (free) energy difference ΔE between the two states is due to the loss of conformational entropy of the coil segments when the ring is located near those segments. If we denote the single segment partition function with and without ring as Z_1 and Z_0, respectively, the energy difference is then given by

$$\Delta E = -k_BT \ln \frac{Z_1^2}{Z_0^2} = -2k_BT \ln \frac{Z_1}{Z_0} \tag{8}$$

Considering the physical meaning of Z_0 and Z_1, we can readily conclude that ΔE is independent of α since Z_0 and Z_1 are both local quantities and should not depend on the rod/coil length ratio, i.e., α. This prediction is confirmed in Figure 4a, which plots $\Delta E/k_BT$ as a function of α for different values of μ. Furthermore, the physical meanings of Z_0 and Z_1 also imply that ΔE must depend on the parameter μ, which quantifies the stretching degree of the coil block. This stretching effect could be explained qualitatively by using the freely jointed chain model of polymers despite the fact that the excluded volume interactions are present in our simulation model. The ideal chain model can be seen as an approximation of the simulation model, which could provide a qualitative understanding of the simulation results. Employing an ideal chain model here could also be justified to some extent by a fact that the excluded volume interactions become more and more irrelevant as the coil chain is stretched,[88−90] since according to the mean-field picture (i.e., Flory theory[4]) of a polymer in a good solvent, strength of the excluded volume interaction is inversely proportional to the pervaded volume of the chain.[4] Consequently, here, we adopt the simplest model of a freely joined chain to leverage the following analytic results. As an ideal picture, we assume that the PR backbone is along the z axis, and there are three consecutive chain segments $i-1$, i, and $i+1$ on the coil block as schematically shown in Figure 4b. Using a spherical coordinate system, the orientation of the bond vector of $\vec{r}_{i+1} - \vec{r}_i$ is described by two angular variables, θ and ω, as shown in Figure 3b. When the ring is absent from this chain segment and when the coil is not

https://doi.org/10.1021/acs.macromol.3c01805
Macromolecules 2024, 57, 1846−1858

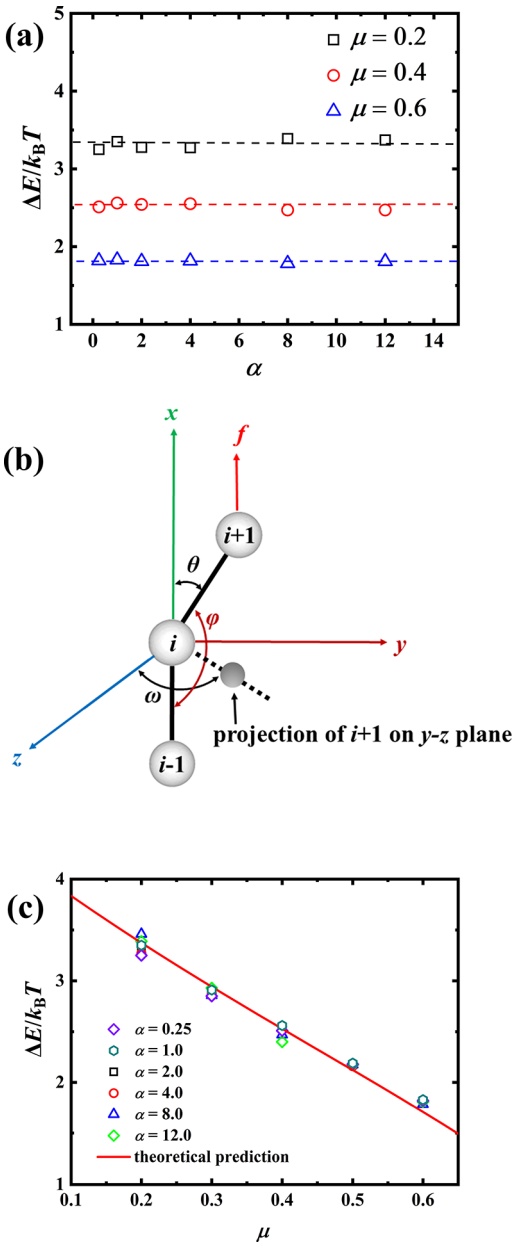

Figure 4. (a) Relationship between energy difference $\Delta E/k_BT$ and the rod/coil ratio α for different values of μ in the single ring-threaded PR system. The dashed lines are guides of the eye. (b) Schematics of three consecutive chain segments $i-1$, i, and $i+1$ on the coil strand of PR. (c) Relationship between $\Delta E/k_BT$ and the parameter μ with different values of α. The red line is the theoretical prediction according to eqs 12 and 13. Notably, the parameters of all systems as used in subfigures (a) and (c) are shown in Table S4 of the Supporting Information.

stretched, the value of θ can cover a range from 0 to π while ω from 0 to 2π, in accordance with the freely jointed chain model. Thus, the partition function for Bead $(i+1)$ could be obtained as

$$Z_0 = \int_0^{\pi} \sin\theta d\theta \int_0^{2\pi} d\omega = 4\pi \tag{9}$$

On the other hand, when this segment is occupied by the ring, the motion of Bead $(i+1)$ should be affected by the excluded volume interaction from the ring. In this case, the largest value of θ should decrease from π to a smaller value, θ_0. In this case, the partition function for Bead $(i+1)$ turns out to be

$$Z_1 = \int_0^{\theta_0} \sin\theta d\theta \int_0^{2\pi} d\omega = 2\pi(1-\cos\theta_0) \tag{10}$$

Next, we consider the effect of μ to be equivalent as the coil is stretched. This can be modeled as an imposed external force f along the chain backbone, i.e., along z axis. In general, consistency between statistical mechanical properties of a polymer chain by a constant pulling force and the case of a chain with a constant extension only holds in the thermodynamic limit, due to the equivalence of ensembles in statistical mechanics.[91] Nevertheless, as Wang[92] pointed out, this equivalence holds for any N in the case of ideal chains because of the statistical independence of the different degrees of freedom in such case. Thus, the probability of the configuration of Bead $(i+1)$ (shown in Figure 4b) under a stretching force f could be written as $p(\theta) \sim e^{fb\cos\theta/k_BT}$, and the partition function for Bead $(i+1)$ should be

$$\begin{aligned} Z_1 &= \int_0^{\theta_0} \sin\theta e^{fb\cos\theta/k_BT} d\theta \int_0^{2\pi} d\omega \\ &= \frac{2\pi k_BT}{fb}(e^{fb/k_BT} - e^{fb\cos\theta_0/k_BT}) \end{aligned} \tag{11}$$

with b as the bond length. The corresponding Z_0 should be given by

$$\begin{aligned} Z_0 &= \int_0^{\pi} \sin\theta e^{fb\cos\theta/k_BT} d\theta \int_0^{2\pi} d\omega \\ &= \frac{2\pi k_BT}{fb}(e^{fb/k_BT} - e^{-fb/k_BT}) \end{aligned} \tag{12}$$

Combining eqs 11 and 12, we obtain an expression of ΔE as

$$\begin{aligned} \Delta E &= -2k_BT \ln(Z_1/Z_0) \\ &= -2k_BT \ln\frac{e^{fb/k_BT} - e^{fb\cos\theta_0/k_BT}}{e^{fb/k_BT} - e^{-fb/k_BT}} \end{aligned} \tag{13}$$

This equation provides the relationship between ΔE and applied force f. For the freely jointed chain model considered here, the applied force, f, can be quantitatively related to the end-to-end distance of the chain, R_{ee}, which is one of the controlling parameter in our simulation model, through the Langevin function[4]

$$R_{ee} = bN\left[\coth\left(\frac{fb}{k_BT}\right) - \frac{1}{fb/(k_BT)}\right] \tag{14}$$

Recalling the definition of $\mu \approx R_{ee}/N_i b$, we can now derive a theoretical relationship between ΔE and μ by the combination of eqs 12 and 13. The symbols shown in Figure 4c represent the values of ΔE obtained from MD simulations plotted as a function of μ. The collapse of the data for different values of α again proves that ΔE is independent of α, which is in agreement with the result of Figures 2a and 4a. Furthermore, the theoretical prediction with θ_0 as the only fitting parameter is given as a solid red line in Figure 4c. In practice, a value of $\theta_0 = 39.5°$ is obtained by fitting the theory to the simulation data. Actually, one could also estimate the value of θ_0 through a geometric analysis with the excluded volumes of the coil segments and the ring segments being considered (see Figure

https://doi.org/10.1021/acs.macromol.3c01805
Macromolecules 2024, 57, 1846−1858

S1 in the Supporting Information), which gives $\theta_0 = 38°$. This consistency of θ_0 suggests that the main physics behind the energy gap ΔE has been retained within the theoretical argument proposed here. The theoretical prediction is consistent with the MD simulation results. It arrives at the conclusion that the free energy difference ΔE is indeed a function of μ, i.e., $\Delta E = \Delta E(\mu)$.

Because the parameter μ characterizes the extension of the coil block, its effect is equivalent to the stretching degree of the coil block, which can be quantified by the averaged bending angle, $\langle\varphi\rangle$, of the segments of the coil block. Furthermore, the effect of the excluded volume interactions between polymer segments could also be effectively captured by the freely rotating chain model.[93,94] According to the freely rotating chain model,[4] the mean-square end-to-end distance is related to the average bending angle, $R_{ee} \approx C_\infty N_f l_0^2$, with $C_\infty = \frac{1-\cos\langle\varphi\rangle}{1+\cos\langle\varphi\rangle}$ being the Flory characteristic ratio of the chain. In our case, the bending angle parameter, φ, is defined by the angle formed by three consecutive beads on the backbone. Therefore, the dependence of ΔE on μ is translated into a dependence on $\langle\varphi\rangle$, i.e., $\Delta E = \Delta E(\langle\ \varphi\ \rangle)$. This prediction is confirmed by simulations from the single ring-threaded PR system shown in Figure 5a, where ΔE values obtained from various rod−coil−rod PR systems are plotted as a function of their corresponding bending angle $\langle\varphi\rangle$ of the coil.

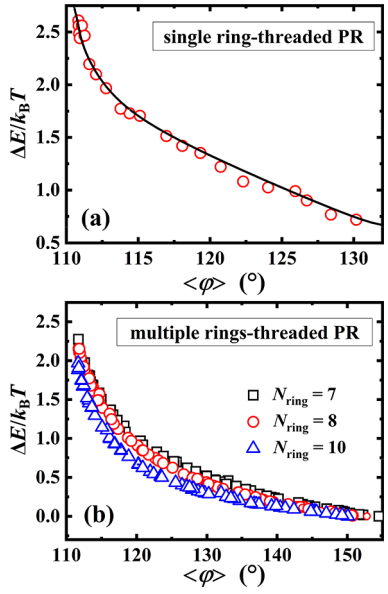

Figure 5. Relationship between energy difference $\Delta E/k_BT$ and the angular parameter $\langle\varphi\rangle$ for (a) single ring-threaded PR and (b) multiple ring-threaded PR with different sizes of ring N_{ring}. The black line in subsection (a) is a guide for the eyes.

The above results were obtained for a rod−coil−rod PR with one threaded ring. It is interesting to see whether the proposed theoretical argument applies to the system of a rod−coil−rod PR threaded with multiple rings. To this end, we compute the energy gap ΔE and the average bending angle $\langle\varphi\rangle$ and plot them together in Figure 5b. It is obvious that these two quantities are correlated with each other through a functional form similar to that obtained for the case of one threaded ring. For elucidating the cause for the decrease of ΔE with an increased value of $\langle\varphi\rangle$ in the multiple ring-threaded PR system, we need first clarify the influence of threaded ring density ρ_{ring} on the backbone flexibility. Previous experimental studies[95,96] have revealed that increasing the ring coverage in PRs (ρ_{ring}) leads to a stiffer PR conformation, i.e., equivalently larger value of the average bending angle parameter $\langle\varphi\rangle$. We stress that since ρ_{ring} quantifies the density (or coverage) of rings, more coated rings inevitably change the rigidity of the axial polymer. Therefore, we may expect a monotonic dependence of $\langle\varphi\rangle$ on ρ_{ring}, i.e., increasing ρ_{ring} should lead to the increase of $\langle\varphi\rangle$. For validating it, we perform a simulation in which the PR axial polymer involves only the coil block, i.e., $N_r = 0$ and $N = N_f$ so that the whole polymer backbone is flexible. Figure 6 shows the dependence of the

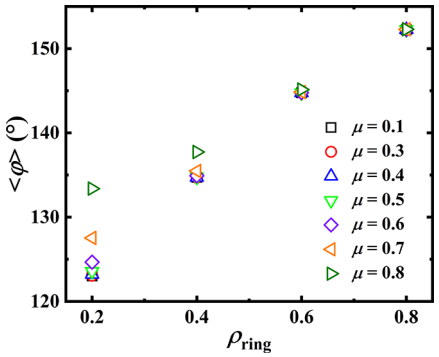

Figure 6. Dependence of the averaged bending angle parameter $\langle\varphi\rangle$ for the flexible axial polymer on the density of threaded rings ρ_{ring} in conditions with $\mu = 0.1-0.8$.

averaged bending angle $\langle\varphi\rangle$ on the ring density ρ_{ring}. It is clear that, for both the conditions with obviously stretched (e.g., $\mu = 0.8$) and less stretched (e.g., $\mu = 0.1$) polymer backbone, we can find monotonic increase of $\langle\varphi\rangle$ on increasing ρ_{ring}, which verifies the above speculation. In addition, we find that, for the plots with different μ, they show relatively large difference in the region of small ρ_{ring} but almost overlap with each other at large ρ_{ring}. It implies that when the ring coverage is low, i.e., with small ρ_{ring}, the intrinsic stretchability of the axial polymer dominantly determines the bending angle parameter $\langle\varphi\rangle$. However, under the condition that the axial polymer is almost fully covered with rings, i.e., with quite large ρ_{ring}, it shows the similar flexibility and is independent of its intrinsic stretchability μ. It is easy to understand that when the ring coverage is high enough, the bending angle parameter $\langle\varphi\rangle$ is more dependent on its local flexibility. When its local segment is fully covered with rings, the flexibility should show no difference. In this study, the ring coverage is simply given by the parameter ρ_{ring}. With the above analysis, the decrease of ΔE with increased value of $\langle\varphi\rangle$ can be attributed to the fact that increasing the ring coverage leads to a stiffer PR chain, thus a larger value of $\langle\varphi\rangle$. Combining all the observations from our simulations, we arrive at a conclusion that the energy gap has the dependence of ρ_{ring} that $\Delta E = \Delta E(\langle\ \varphi\ \rangle) = \Delta E(\mu, \rho_{ring})$.

3.1.2. Globally Entropic Loss of the Coil Strand. The excluded volume interactions between the rings and the coil segments, which are far apart from the ring's location along the PR backbone, may come into effect when the relative extension of the coil block μ becomes relatively smaller, leading to an entropic cost of the coil chain. Quantitatively, the entropic loss of a coil chain can be measured in terms of the excluded

https://doi.org/10.1021/acs.macromol.3c01805
Macromolecules 2024, 57, 1846−1858

volume interaction.[2,97] In this section, we endeavor to obtain a qualitative understanding of the effect of the ratio of the rod to the coil strand lengths α on the energy gap ΔE when the relative extension of the coil block μ becomes relatively smaller as shown in Figure 2. Within a mean-field approximation, the excluded volume interaction of the coil strand without threaded rings is given by

$$F_{\text{int}} \approx k_{\text{B}}Tv_0\frac{N_{\text{f}}^2}{R_{\text{g}}^3}, \tag{15}$$

in which v_0 denotes the excluded volume of each coil segment, and R_{g} is the gyration radius of the coil chain with N_{f} segments. We assume $R_{\text{g}} \simeq R_{\text{ee}}$ with $R_{\text{ee}} = \mu R_{\text{max}} \sim \mu N_{\text{f}}$. Then, we have

$$F_{\text{int}} \sim \frac{k_{\text{B}}Tv_0}{\mu^3 N_{\text{f}}} \tag{16}$$

When the coil strand is threaded by one ring, the excluded volume interaction can be similarly derived as

$$F'_{\text{int}} \approx k_{\text{B}}Tv_0\frac{(N_{\text{f}}+N_{\text{ring}})^2}{R_{\text{g}}^3} \sim k_{\text{B}}Tv_0\left[\frac{1}{\mu^3 N_{\text{f}}}+\frac{2N_{\text{ring}}}{\mu^3 N_{\text{f}}^2}\right] \tag{17}$$

where $R_{\text{g}} \simeq R_{\text{ee}} \sim \mu N_{\text{f}}$ is again used. The energy difference between the above two states of the coil approximately may give a rough estimate of ΔE for the single-ring system:

$$\Delta E \approx F'_{\text{int}} - F_{\text{int}} \sim k_{\text{B}}Tv_0\frac{2N_{\text{ring}}}{\mu^3 N_{\text{f}}^2} \tag{18}$$

Recalling $2N_{\text{r}}/N_{\text{f}} = \alpha$ and $N = 2N_{\text{r}} + N_{\text{f}}$ gives $N_{\text{f}} = N/(1+\alpha)$. Then, we arrive at

$$\Delta E \sim \frac{(1+\alpha)^2}{\mu^3} \tag{19}$$

This mean-field prediction eq 19 also holds for the case of the multiple ring systems as long as the excluded volume interactions between the rings can be ignored, i.e., when ρ_{ring} is small. The conclusion from eq 19 that ΔE is inversely proportional to μ but proportional to α is qualitatively consistent with the results shown in Figure 2a,b.

3.2. Sliding Dynamics of Rings along the PR Backbone. Now we look into the consequences of the energy gap ΔE in the sliding dynamics of rings along the rod−coil−rod PR backbone. According to the transition state theory, once the energy barrier is larger than the thermal energy, transition events between the two involved states would be increasingly rare in which the transition time is exponentially dependent on the energy barrier. Consequently, in current case, there could be a hopping event of rings sliding from the rod to the coil strands emerged when $\frac{\Delta E}{k_{\text{B}}T} > 1$. We will examine this theoretical prediction in simulations of single-ring rod−coil−rod PR systems. Let us denote the time of a ring sliding from the rod block to the coil one as τ_{p}. For the system with single-ring threaded PR, when the ring is located anywhere on the rod block, we record the time point as t_0. Then, the ring starts sliding along the backbone chain via Brownian motion and hops to the coil block at t_1, i.e., the hopping time is recorded as $\tau_{\text{p}} = t_1 - t_0$. After achieving a successful hopping from the rod to the coil, the ring is placed randomly on the rod block again and starts a new attempt for sliding. We carried out a sufficiently large number of simulations for the calculation of the averaged hopping time $\langle\tau_{\text{p}}\rangle$. According to the transition state theory, $\langle\tau_{\text{p}}\rangle$ should be linked to ΔE by

$$\langle\tau_{\text{p}}\rangle = \tau_0 \exp\left(\frac{\Delta E}{k_{\text{B}}T}\right) \tag{20}$$

Here, the value τ_0 corresponds to the relaxation time of the ring on the rod block of PR. Equivalently, this equation can be rewritten as

$$\ln\left(\frac{\langle\tau_{\text{p}}\rangle}{\tau_0}\right) = \Delta E/k_{\text{B}}T \tag{21}$$

This relation (eq 21) has been verified in our simulation results as shown in Figure 7a, where there is a single ring

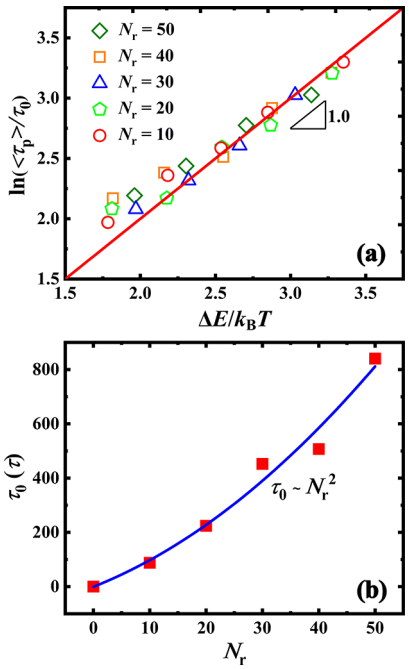

Figure 7. (a) Semilog relationship between the rescaled hopping time $\ln(\langle\tau_{\text{p}}\rangle/\tau_0)$ and the energy difference $\Delta E/k_{\text{B}}T$ in the single-ring PR system. (b) Dependence of relaxation time τ_0 on the rod block length N_{r} in the system with single-threaded ring (the red scatters). The blue curve shows the fitting of the scatters with a quadratic function of $\tau_0 \sim N_{\text{r}}^2$.

sliding along the PR backbones with varying rod block length as $N_{\text{r}} = 10-50$. Figure 7b shows the dependence of τ_0 on the chain length of rod block N_{r} (the red scatters). It is found that τ_0 is quadratically proportional to N_{r}, i.e., $\tau_0 \sim N_{\text{r}}^2$ (fitting by the blue curve). This finding is in excellent agreement with the fact that rings are under a Brownian motion along the PR backbone and suggests that the physical meaning of τ_0 could be the passing time of a ring along the rod strand via Brownian dynamics.

Next, the features of ring hopping in a multiple ring-threaded PR system are also investigated. In this section, the dependence of the hopping frequency, which is measured by the average number of hopping events of rings per unit time, $\overline{n}_{\text{hop}}$, on the system parameters μ and ρ_{ring} are studied. First, we consider the effect of the ring coverage ρ_{ring} on the hopping behavior of rings. Without loss of generality, we choose a series of PR systems with fixed parameters ($\alpha = 0.5$ and $\mu = 0.4$). By varying the values of N_{f} and N_{r}, or simply tuning the number of

https://doi.org/10.1021/acs.macromol.3c01805
Macromolecules 2024, 57, 1846−1858

threaded rings n_{ring} on PR, we can obtain PR systems with different values of ρ_{ring}. In Figure 8a, we show the dependence

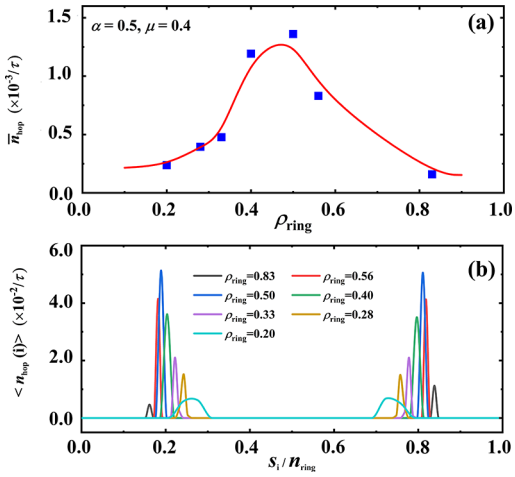

Figure 8. (a) Dependence of mean count of hopping events in unit time of rings $\overline{n}_{hop}$ on the ring coverage density ρ_{ring} in the multiple ring-threaded PR system with $\alpha = 0.5$ and $\mu = 0.4$ (blue scatters). The red curve is for guiding the line. (b) The distribution of hopping event counts in unit time $\langle n_{hop}(i)\rangle$ of rings on the PR backbone for the systems in (a) with different ρ_{ring}. Here, n_{ring} is the total number of rings, while S_i denotes the index of the i-th ring. Notably, the parameters of all systems as used in this figure are shown in Table S5 of the Supporting Information.

of $\overline{n}_{hop}$ of all rings on ring coverage density ρ_{ring}. It is revealed that with the increase in ρ_{ring} at the region of $\rho_{ring} = 0.2-0.5$, $\overline{n}_{hop}$ increases remarkably with increasing ρ_{ring}. When $\rho_{ring} > 0.5$, however, $\overline{n}_{hop}$ decreases gradually as ρ_{ring} increases. This finding can be explained in the following. When the ring coverage is low (e.g., $\rho_{ring} < 0.5$), rings are so sparsely distributed along the PR backbone that they can undergo sliding motion via Brownian dynamics. Increasing the number of rings (thus increasing ρ_{ring}) in this situation would enhance the frequency of ring collision along the rod strand and thereafter activate more hopping events happening. For the PR systems with larger ring coverage (e.g., $\rho_{ring} > 0.5$), however, rings become nearly frozen along the PR backbone; i.e., ring sliding is significantly suppressed, leading to a depression of the effective ring colliding. Therefore, the number of hopping events of rings per unit time, $\overline{n}_{hop}$, is further decreased with further increasing ρ_{ring}.

For exploring the detailed contributions of hopping of each ring to the (total) number of hopping events $\overline{n}_{hop}$ given in Figure 8a, we further investigate the average number of hopping events of every ring on the PR backbone per unit time. To this end, the number of hopping events of the i-th ring along the PR backbone per unit time, $\langle n_{hop}(i)\rangle$, is shown in Figure 8b, where S_i is the index of the i-th ring. For all cases with different ρ_{ring}, we observe a bimodal distribution of $\langle n_{hop}(i)\rangle$ in specific regions of S_i/n_{ring} being nonzero while in other regions $\langle n_{hop}(i)\rangle = 0$. This fact reveals that only those rings located near the rod−coil strand boundary can hop from the rod to the coil strands. For the case of $\rho_{ring} = 0.2$, the distributions of $\langle n_{hop}(i)\rangle$ are relatively broad, indicating that more rings near the rod−coil boundary are active on hopping. With the increase of ρ_{ring}, the distributions turn to be sharper, and meanwhile, their peaks become higher. For systems with further increasing ρ_{ring} (e.g., when $\rho_{ring} > 0.5$), the bimodal peaks are apparently lower, which is consistent with the hindered hopping events due to the increasing frozen rings along the PR backbone. Notably, to better understand the exclusive impact of coil segment length on the ring hopping dynamics, we specifically design a comparison in which the effect ascribed from the variation of coil segment length on the hopping dynamics can be presented. See Figure S3 and the corresponding discussions in the Supporting Information (Section 3 of Supporting Information).

The dependence of the number of hopping events of rings per unit time $\overline{n}_{hop}$ on the parameters μ is shown in Figure 9a.

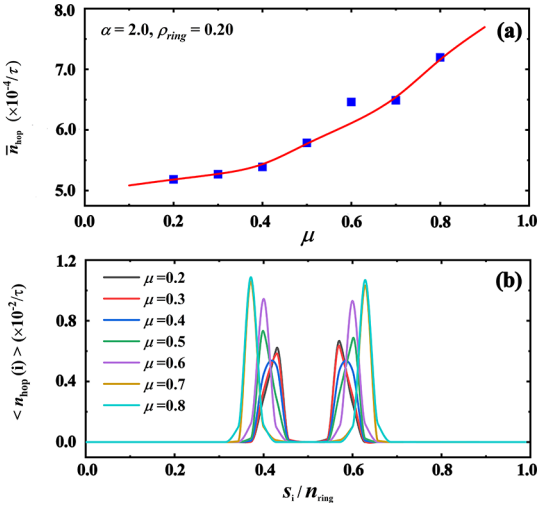

Figure 9. (a) Dependence of the mean count of hopping events in unit time of rings $\overline{n}_{hop}$ on the parameter μ in the multiple ring-threaded PR system with $\alpha = 2.0$ and $\rho_{ring} = 0.2$ (blue scatters). The red curve is for guiding the line. (b) Distribution of hopping event counts in unit time $\langle n_{hop}(i)\rangle$ of all rings on the PR backbone for the systems in (a) with different μ. Notably, the parameters of all systems as used in this figure are shown in Table S6 of Supporting Information.

For simplicity, we choose systems with the parameters $\alpha = 2.0$ and $\rho_{ring} = 0.2$ for demonstration. By fixing $N_r = N_f$ but changing R_{ee} of the coil strand (see schematics in Figure 1a), we can obtain PR systems with different μ. From Figure 9a, one can easily find a monotonic increase in the plot of $\overline{n}_{hop}$ with respect to μ. Since the ring coverage density is fixed as $\rho_{ring} = 0.2$, the exclusive stretching of the coil strand (corresponding to the increase of μ) could yield the continuous decrease of the free energy difference ΔE, according to the result of Figure 2b. Consequently, more rings should become active on hopping events with decreased ΔE.

Similarly, for analyzing the contributions of each ring on $\overline{n}_{hop}$ in Figure 9a, we also plot the distribution of $\langle n_{hop}(i)\rangle$ of all threaded rings, as shown in Figure 9b. We can find a similar bimodal distribution of $\langle n_{hop}(i)\rangle$ symmetrically centered with $S_i/n_{ring} = 0.5$, as that in Figure 8b. Moreover, for the systems with smaller μ, the bimodal peaks stay closer to the center $S_i/n_{ring} = 0.5$. It is ascribed to the fact that, because of the increased ΔE with smaller μ, only a few rings could stay on the coil strand (the ones with index S_i/n_{ring} close to 0.5), while most ones are on the rod block. Therefore, the rings which can frequently hop up and down at the rod−coil boundary should be the ones with their indexes relatively near the innermost ring (the center ring) as well; i.e., the bimodal peaks appear

https://doi.org/10.1021/acs.macromol.3c01805
Macromolecules 2024, 57, 1846−1858

close to the center $S_i/n_{ring} = 0.5$. In contrast, with the increase of μ, the bimodal peaks separate with each other even farther on the x-axis, implying that more rings can stay on the coil strand as a result of the obviously decreased free energy difference. Moreover, we also find that with the increase of μ, the bimodal peaks become even higher, but their widths do not turn narrower obviously, which is different from that in Figure 8b. It implies that, based on the same ring coverage density ρ_{ring}, the fraction of rings that are located at the rod−coil boundary and are active on hopping behavior does not change much. Their activities on hopping, however, turn out to be obviously much higher with a larger value of μ (or lower ΔE).

4. CONCLUSIONS

In summary, the entropy-induced localization and sliding dynamics behavior of rings on a PR with a rod−coil−rod backbone have been explored by molecular dynamics simulations. The simulation results revealed that the rings prefer to be located at the rod block regions due to a decrease in the entropy of the coil block. Feature of the ring localization is well described by a two-state system with a free energy gap ΔE. We find that the energy gap is independent of chain length of the backbone and only depends on the three characteristic parameters, $\alpha = 2N_r/N_f$, $\mu = R_{ee}/R_{max}$ and $\rho_{ring} = n_{ring}/N$. This entropic loss is estimated theoretically based on the freely jointed chain model by considering excluded volume interactions between the coil and the ring. Furthermore, the relationship of hopping time of rings with the hopping free energy barrier given by transition state theory is quantitatively verified by simulations. The influence of the parameters μ and ρ_{ring} on the mean count of hopping events of all rings and the distributions of count of hopping for each ring are studied for understanding the feature of ring hopping dynamics. It should be noted that, for a block copolymer as considered, not only the stiffness but also the chemical nature of the blocks will be different. This might also have a large impact on the distribution of the rings and on their dynamics as the entropic effect due to the different flexibility. In addition, the solvent conditions will also affect the rotaxane−rings interaction, which further impacts the dynamics. For emphasizing the regulation of threaded rings mediated by the entropy effect, we have to decouple all of the above factors in this study. Those effects including solvent quality and chemical differences of blocks deserve to be studied in the following investigations. The coupling of different effects should trigger various regulation results of rings localized on the PR.

■ ASSOCIATED CONTENT

Supporting Information

The Supporting Information is available free of charge at https://pubs.acs.org/doi/10.1021/acs.macromol.3c01805.

Schematics of the geometric relationship between the ring beads and the coil strand beads; impact of polymer thickness on ΔE; hopping dynamics of rings with varying the length of coil strand; parameters used for simulated models in the manuscript, Figures 2, 4, 8, and 9 (PDF)

■ AUTHOR INFORMATION

Corresponding Authors

An-Chang Shi − *Department of Physics & Astronomy, McMaster University, Hamilton, Ontario L8M 4S1, Canada;* orcid.org/0000-0003-1379-7162; Email: shi@mcmaster.ca

Jiajia Zhou − *South China Advanced Institute for Soft Matter Science and Technology, School of Emergent Soft Matter, South China University of Technology, Guangzhou 510640, China;* orcid.org/0000-0002-2258-6757; Email: zhouj2@scut.edu.cn

Guojie Zhang − *School of Chemistry and Chemical Engineering, Guangzhou University, Guangzhou 510006, China*; Email: guojie.zhang@gzhu.edu.cn

Hong Liu − *Key Laboratory of Theoretical Chemistry of Environment Ministry of Education, School of Environment and Guangdong Provincial Key Laboratory of Chemical Pollution and Environmental Safety, South China Normal University, Guangzhou 510006, China;* orcid.org/0000-0002-7256-5751; Email: hongliu@m.scnu.edu.cn

Authors

Yan Wang − *Key Laboratory of Theoretical Chemistry of Environment Ministry of Education, School of Environment, South China Normal University, Guangzhou 510006, China;* orcid.org/0000-0002-9003-8680

Hui Lu − *Key Laboratory of Theoretical Chemistry of Environment Ministry of Education, School of Environment, South China Normal University, Guangzhou 510006, China; Xuzhou No.35 Middle School, Xuzhou 221003, China;* orcid.org/0000-0003-1681-0166

Xiang-Meng Jia − *South China Advanced Institute for Soft Matter Science and Technology, School of Emergent Soft Matter, South China University of Technology, Guangzhou 510640, China;* orcid.org/0000-0002-4056-747X

Complete contact information is available at: https://pubs.acs.org/10.1021/acs.macromol.3c01805

Author Contributions

Y.W., H.L., and X.-M.J. contributed equally.

Notes

The authors declare no competing financial interest.

■ ACKNOWLEDGMENTS

Valuable comments and suggestions from Prof. Dr. Marcus Müller of Georg-August-Universität Göttingen and Prof. Dr. Pengfei Zhang from Donghua University are greatly appreciated. This work is supported by the Open Research Fund of Songshan Lake Materials Laboratory (2023SLABFK11) and the National Natural Science Foundation of China (22273027, 21873023, 22022303). H.L. gratefully acknowledges the support from the Alexander von Humboldt Foundation. Authors acknowledge anonymous refrees for their insightful comments.

■ REFERENCES

(1) Khokhlov, A. R.; Grosberg, A. Y.; Pande, V. S. *Statistical physics of macromolecules*; Springer, 1994.
(2) De Gennes, P.-G. *Scaling concepts in polymer physics*; Cornell University Press, 1979.
(3) Doi, M.; Edwards, S. *The theory of polymer dynamics*; Oxford University Press (Clarendon): London, New York, 1986.
(4) Rubinstein, M.; Colby, R. *Polymer Physics*; Oxford University Press, 2003.
(5) Strobl, G. R. *The physics of polymers*; Springer, 1997.
(6) Niu, Z.; Gibson, H. W. Polycatenanes. *Chem. Rev.* **2009**, *109* (11), 6024−6046.

(7) Gibson, H. W.; Bheda, M. C.; Engen, P. T. Rotaxanes, catenanes, polyrotaxanes, polycatenanes and related materials. *Prog. Polym. Sci.* **1994**, *19* (5), 843−945.
(8) Huang, F.; Gibson, H. W. Polypseudorotaxanes and polyrotaxanes. *Prog. Polym. Sci.* **2005**, *30* (10), 982−1018.
(9) Harada, A.; Hashidzume, A.; Yamaguchi, H.; Takashima, Y. Polymeric rotaxanes. *Chem. Rev.* **2009**, *109* (11), 5974−6023.
(10) Arunachalam, M.; Gibson, H. W. Recent developments in polypseudorotaxanes and polyrotaxanes. *Prog. Polym. Sci.* **2014**, *39* (6), 1043−1073.
(11) Hart, L. F.; Hertzog, J. E.; Rauscher, P. M.; Rawe, B. W.; Tranquilli, M. M.; Rowan, S. J. Material properties and applications of mechanically interlocked polymers. *Nat. Rev. Mater.* **2021**, *6* (6), 508−530.
(12) Wikoff, W. R.; Liljas, L.; Duda, R. L.; Tsuruta, H.; Hendrix, R. W.; Johnson, J. E. Topologically linked protein rings in the bacteriophage HK97 capsid. *Science* **2000**, *289* (5487), 2129−2133.
(13) Lee, B. I.; Kim, K. H.; Park, S. J.; Eom, S. H.; Song, H. K.; Suh, S. W. Ring-shaped architecture of RecR: implications for its role in homologous recombinational DNA repair. *EMBO J.* **2004**, *23* (10), 2029−2038.
(14) Cao, Z.; Roszak, A. W.; Gourlay, L. J.; Lindsay, J. G.; Isaacs, N. W. Bovine mitochondrial peroxiredoxin III forms a two-ring catenane. *Structure* **2005**, *13* (11), 1661−1664.
(15) Boutz, D. R.; Cascio, D.; Whitelegge, J.; Perry, L. J.; Yeates, T. O. Discovery of a thermophilic protein complex stabilized by topologically interlinked chains. *J. Mol. Biol.* **2007**, *368* (5), 1332−1344.
(16) Zimanyi, C. M.; Ando, N.; Brignole, E. J.; Asturias, F. J.; Stubbe, J.; Drennan, C. L. Tangled up in knots: structures of inactivated forms of E. coli class Ia ribonucleotide reductase. *Structure* **2012**, *20* (8), 1374−1383.
(17) Van Eldijk, M. B.; Van Leeuwen, I.; Mikhailov, V. A.; Neijenhuis, L.; Harhangi, H. R.; Van Hest, J. C.; Jetten, M. S.; Den Camp, H. J. O.; Robinson, C. V.; Mecinović, J. Evidence that the catenane form of CS_2 hydrolase is not an artefact. *Chem. Commun.* **2013**, *49* (71), 7770−7772.
(18) Aguirre, C.; Goto, Y.; Costas, M. Thermal and chemical unfolding pathways of PaSdsA1 sulfatase, a homo-dimer with topologically interlinked chains. *FEBS Lett.* **2016**, *590* (2), 202−214.
(19) Pieters, B. J.; Van Eldijk, M. B.; Nolte, R. J.; Mecinović, J. Natural supramolecular protein assemblies. *Chem. Soc. Rev.* **2016**, *45* (1), 24−39.
(20) Domínguez-Gil, T.; Molina, R.; Dik, D. A.; Spink, E.; Mobashery, S.; Hermoso, J. A. X-ray structure of catenated lytic transglycosylase SltB1. *Biochemistry* **2017**, *56* (48), 6317−6320.
(21) Hudson, B.; Vinograd, J. Catenated circular DNA molecules in HeLa cell mitochondria. *Nature* **1967**, *216* (5116), 647−652.
(22) Clayton, D. A.; Vinograd, J. Circular dimer and catenate forms of mitochondrial DNA in human leukaemic leucocytes. *Nature* **1967**, *216* (5116), 652−657.
(23) Gibson, H. W.; Nagvekar, D. S.; Yamaguchi, N.; Bhattacharjee, S.; Wang, H.; Vergne, M. J.; Hercules, D. M. Polyamide Pseudorotaxanes, Rotaxanes, and Catenanes Based on Bis (5-carboxy-1, 3-phenylene)-(3x+2)-crown-x Ethers. *Macromolecules* **2004**, *37* (20), 7514−7529.
(24) Fustin, C.-A.; Clarkson, G.; Leigh, D.; Van Hoof, F.; Jonas, A. M.; Bailly, C. Mechanically linked poly (ethylene terephthalate). *Macromolecules* **2004**, *37* (21), 7884−7892.
(25) Berrocal, J. A.; Pitet, L. M.; Nieuwenhuizen, M. M.; Mandolini, L.; Meijer, E.; Di Stefano, S. Ring-opening metathesis polymerization of a diolefinic [2]-catenane−copper (I) complex: an easy route to polycatenanes. *Macromolecules* **2015**, *48* (5), 1358−1363.
(26) Cao, P.-F.; Mangadlao, J. D.; de Leon, A.; Su, Z.; Advincula, R. C. Catenated poly (*ε*-caprolactone) and poly (l-lactide) via ring-expansion strategy. *Macromolecules* **2015**, *48* (12), 3825−3833.
(27) Lu, C. H.; Qi, X. J.; Cecconello, A.; Jester, S. S.; Famulok, M.; Willner, I. Switchable reconfiguration of an interlocked DNA olympiadane nanostructure. *Angew. Chem., Int. Ed.* **2014**, *53* (29), 7499−7503.
(28) Jester, S.-S.; Famulok, M. Mechanically interlocked DNA nanostructures for functional devices. *Acc. Chem. Res.* **2014**, *47* (6), 1700−1709.
(29) Wang, X. W.; Zhang, W. B. Cellular synthesis of protein catenanes. *Angew. Chem., Int. Ed.* **2016**, *55* (10), 3442−3446.
(30) Sawada, T.; Yamagami, M.; Ohara, K.; Yamaguchi, K.; Fujita, M. Peptide [4] catenane by folding and assembly. *Angew. Chem., Int. Ed.* **2016**, *55* (14), 4519−4522.
(31) Allen, C. D.; Link, A. J. Self-assembly of catenanes from lasso peptides. *J. Am. Chem. Soc.* **2016**, *138* (43), 14214−14217.
(32) Liu, D.; Wu, W.-H.; Liu, Y.-J.; Wu, X.-L.; Cao, Y.; Song, B.; Li, X.; Zhang, W.-B. Topology engineering of proteins in vivo using genetically encoded, mechanically interlocking SpyX modules for enhanced stability. *ACS Cent. Sci.* **2017**, *3* (5), 473−481.
(33) Wang, X.-W.; Zhang, W.-B. Chemical topology and complexity of protein architectures. *Trends Biochem. Sci.* **2018**, *43* (10), 806−817.
(34) Wu, Q.; Rauscher, P. M.; Lang, X.; Wojtecki, R. J.; De Pablo, J. J.; Hore, M. J.; Rowan, S. J. Poly[n]catenanes: Synthesis of molecular interlocked chains. *Science* **2017**, *358* (6369), 1434−1439.
(35) Kato, K.; Ohara, A.; Yokoyama, H.; Ito, K. Prolonged glass transition due to topological constraints in polyrotaxanes. *J. Am. Chem. Soc.* **2019**, *141* (32), 12502−12506.
(36) Zhang, Z.; Hou, G.; Shen, J.; Liu, J.; Gao, Y.; Zhao, X.; Zhang, L. Designing the Slide-Ring Polymer Network with Both Good Mechanical and Damping Properties via Molecular Dynamics Simulation. *Polymers* **2018**, *10*, 964.
(37) Xing, H.; Li, Z.; Wang, W.; Liu, P.; Liu, J.; Song, Y.; Wu, Z. L.; Zhang, W.; Huang, F. Mechanochemistry of an interlocked poly [2] catenane: from single molecule to bulk gel. *CCS Chemistry* **2020**, *2* (1), 513−523.
(38) Zhang, Z.; Cheng, L.; Zhao, J.; Wang, L.; Liu, K.; Yu, W.; Yan, X. Synergistic covalent and supramolecular polymers for mechanically robust but dynamic materials. *Angew. Chem., Int. Ed.* **2020**, *59* (29), 12139−12146.
(39) Li, G.; Wang, L.; Wu, L.; Guo, Z.; Zhao, J.; Liu, Y.; Bai, R.; Yan, X. Woven polymer networks via the topological transformation of a [2] catenane. *J. Am. Chem. Soc.* **2020**, *142* (33), 14343−14349.
(40) Zhao, D.; Zhang, Z.; Zhao, J.; Liu, K.; Liu, Y.; Li, G.; Zhang, X.; Bai, R.; Yang, X.; Yan, X. A mortise-and-tenon joint inspired mechanically interlocked network. *Angew. Chem., Int. Ed.* **2021**, *60* (29), 16224−16229.
(41) Liu, C.; Morimoto, N.; Jiang, L.; Kawahara, S.; Noritomi, T.; Yokoyama, H.; Mayumi, K.; Ito, K. Tough hydrogels with rapid self-reinforcement. *Science* **2021**, *372* (6546), 1078−1081.
(42) Gavrilov, A. A.; Potemkin, I. I. Adaptive structure of gels and microgels with sliding cross-links: enhanced softness, stretchability and permeability. *Soft Matter* **2018**, *14* (24), 5098−5105.
(43) Balzani, V.; Credi, A.; Raymo, F. M.; Stoddart, J. F. Artificial molecular machines. *Angew. Chem., Int. Ed.* **2000**, *39* (19), 3348−3391.
(44) Stoddart, J. F. Mechanically interlocked molecules (MIMs)—molecular shuttles, switches, and machines (Nobel Lecture). *Angew. Chem., Int. Ed.* **2017**, *56* (37), 11094−11125.
(45) Sauvage, J. P. From chemical topology to molecular machines (Nobel lecture). *Angew. Chem., Int. Ed.* **2017**, *56* (37), 11080−11093.
(46) Feringa, B. L. The art of building small: From molecular switches to motors (Nobel lecture). *Angew. Chem., Int. Ed.* **2017**, *56* (37), 11060−11078.
(47) Richards, V. Molecular machines. *Nat. Chem.* **2016**, *8* (12), 1090−1090.
(48) Neal, E. A.; Goldup, S. M. Chemical consequences of mechanical bonding in catenanes and rotaxanes: isomerism, modification, catalysis and molecular machines for synthesis. *Chem. Commun.* **2014**, *50* (40), 5128−5142.
(49) Evans, N. H.; Beer, P. D. Progress in the synthesis and exploitation of catenanes since the Millennium. *Chem. Soc. Rev.* **2014**, *43* (13), 4658−4683.

https://doi.org/10.1021/acs.macromol.3c01805
Macromolecules 2024, 57, 1846−1858

(50) Leigh, D. A.; Marcos, V.; Wilson, M. R. Rotaxane catalysts. *ACS Catal.* **2014**, *4* (12), 4490−4497.
(51) Yasuda, Y.; Toda, M.; Mayumi, K.; Yokoyama, H.; Morita, H.; Ito, K. Sliding dynamics of ring on polymer in rotaxane: A coarse-grained molecular dynamics simulation study. *Macromolecules* **2019**, *52* (10), 3787−3793.
(52) Chen, Z.; Aoki, D.; Uchida, S.; Marubayashi, H.; Nojima, S.; Takata, T. Effect of component mobility on the properties of macromolecular [2] rotaxanes. *Angew. Chem., Int. Ed.* **2016**, *55* (8), 2778−2781.
(53) Fujita, H.; Ooya, T.; Yui, N. Thermally Induced Localization of Cyclodextrins in a Polyrotaxane Consisting of β-Cyclodextrins and Poly (ethylene glycol)−Poly (propylene glycol) Triblock Copolymer. *Macromolecules* **1999**, *32* (8), 2534−2541.
(54) Uenuma, S.; Maeda, R.; Takahashi, S.; Kato, K.; Yokoyama, H.; Ito, K. Self-assembled Structure of Polyrotaxane Consisting of β-Cyclodextrin and Poly (ethylene oxide)-block-poly (propylene oxide)-block-poly (ethylene oxide) Triblock Copolymer in Bulk System. *Chem. Lett.* **2016**, *45* (8), 991−993.
(55) Masai, H.; Oka, Y.; Terao, J. Precision synthesis of linear oligorotaxanes and polyrotaxanes achieving well-defined positions and numbers of cyclic components on the axle. *Chem. Commun.* **2022**, *58* (11), 1644−1660.
(56) Uenuma, S.; Maeda, R.; Kato, K.; Mayumi, K.; Yokoyama, H.; Ito, K. Drastic change of mechanical properties of polyrotaxane bulk: ABA−BAB sequence change depending on ring position. *ACS Macro Lett.* **2019**, *8* (2), 140−144.
(57) Mayumi, K.; Ito, K.; Kato, K. *Polyrotaxane and slide-ring materials*; Royal Society of Chemistry, 2015.
(58) Fujita, H.; Ooya, T.; Yui, N. Synthesis and characterization of a polyrotaxane consisting of β-cyclodextrins and a poly (ethylene glycol)-poly (propylene glycol) triblock copolymer. *Macromol. Chem. Phys.* **1999**, *200* (4), 706−713.
(59) Zhu, S. S.; Swager, T. M. Conducting polymetallorotaxanes: metal ion mediated enhancements in conductivity and charge localization. *J. Am. Chem. Soc.* **1997**, *119* (51), 12568−12577.
(60) Zhu, S. S.; Carroll, P. J.; Swager, T. M. Conducting polymetallorotaxanes: A supramolecular approach to transition metal ion sensors. *J. Am. Chem. Soc.* **1996**, *118* (36), 8713−8714.
(61) Solladié, N.; Chambron, J.-C.; Sauvage, J.-P. Porphyrin-Stoppered [3]- and [5]-Rotaxanes. *J. Am. Chem. Soc.* **1999**, *121* (15), 3684−3692.
(62) Petrukhina, M. A.; Andreini, K. W.; Mack, J.; Scott, L. T. Transition-Metal Complexes of an Open Geodesic Polyarene. *Angew. Chem., Int. Ed.* **2003**, *42* (29), 3375−3379.
(63) Jäger, R.; Händel, M.; Harren, J.; Vögtle, F.; Rissanen, K. Chemistry with Roataxanes: Intra-and Intermolecularly Covalently Linked Rotaxanes. *Liebigs Ann.* **1996**, *7*, 1201−1207.
(64) Reuter, C.; Mohry, A.; Sobanski, A.; Vögtle, F. [1]Rotaxanes and Pretzelanes: Synthesis, Chirality, and Absolute Configuration. *Chem.—Eur. J.* **2000**, *6* (9), 1674−1682.
(65) Arisaka, Y.; Yui, N. Polyrotaxane-based biointerfaces with dynamic biomaterial functions. *J. Mater. Chem. B* **2019**, *7* (13), 2123−2129.
(66) Yui, N.; Ooya, T. Molecular mobility of interlocked structures exploiting new functions of advanced biomaterials. *Chem.—Eur. J.* **2006**, *12* (26), 6730−6737.
(67) Yasuda, Y.; Masumoto, T.; Mayumi, K.; Toda, M.; Yokoyama, H.; Morita, H.; Ito, K. Molecular dynamics simulation and theoretical model of elasticity in slide-ring gels. *ACS Macro Lett.* **2020**, *9* (9), 1280−1285.
(68) Okumura, Y.; Ito, K. The polyrotaxane gel: A topological gel by figure-of-eight cross-links. *Adv. Mater.* **2001**, *13* (7), 485−487.
(69) Müller, T.; Sommer, J.-U.; Lang, M. Tendomers−force sensitive bis-rotaxanes with jump-like deformation behavior. *Soft Matter* **2019**, *15* (18), 3671−3679.
(70) Müller, T.; Sommer, J.-U.; Lang, M. Swelling of Tendomer Gels. *Macromolecules* **2021**, *54* (10), 4601−4614.
(71) Lee, M.; Cho, B.-K.; Zin, W.-C. Supramolecular Structures from Rod−Coil Block Copolymers. *Chem. Rev.* **2001**, *101* (12), 3869−3892.
(72) Ryu, J.-H.; Hong, D.-J.; Lee, M. Aqueous self-assembly of aromatic rod building blocks. *Chem. Commun.* **2008**, *9*, 1043−1054.
(73) Sforazzini, G.; Kahnt, A.; Wykes, M.; Sprafke, J. K.; Brovelli, S.; Montarnal, D.; Meinardi, F.; Cacialli, F.; Beljonne, D.; Albinsson, B.; Anderson, H. L. Synthesis and photophysics of coaxial threaded molecular wires: polyrotaxanes with triarylamine jackets. *J. Phys. Chem. C* **2014**, *118* (8), 4553−4566.
(74) Willis-Fox, N.; Belger, C.; Fennell, J. F., Jr; Evans, R. C.; Swager, T. M. Threading the needle: fluorescent poly-pseudorotaxanes for size-exclusion sensing. *Chem. Mater.* **2016**, *28* (8), 2685−2691.
(75) Ben, L.; Zhou, J.; Ji, H.; Yu, H.; Zhao, W.; Huang, X. Si nanoparticles seeded in carbon-coated Sn nanowires as an anode for high-energy and high-rate lithium-ion batteries. *Materials Futures* **2022**, *1* (1), No. 015101.
(76) Kremer, K.; Grest, G. S. Dynamics of entangled linear polymer melts: A molecular-dynamics simulation. *J. Chem. Phys.* **1990**, *92* (8), 5057−5086.
(77) Weeks, J. D.; Chandler, D.; Andersen, H. C. Role of repulsive forces in determining the equilibrium structure of simple liquids. *J. Chem. Phys.* **1971**, *54* (12), 5237−5247.
(78) Pei, H. W.; Liu, H.; Lu, Z. Y.; Zhu, Y. L. Tuning surface wettability by designing hairy structures. *Phys. Rev. E* **2015**, *91* (2), No. 020401.
(79) Allen, M. P.; Tildesley, D. J. *Computer simulation of liquids*; Oxford University Press, 1987.
(80) Zhu, Y. L.; Liu, H.; Li, Z. W.; Qian, H. J.; Milano, G.; Lu, Z. Y. GALAMOST: GPU-accelerated large-scale molecular simulation toolkit. *J. Comput. Chem.* **2013**, *34* (25), 2197−2211.
(81) Dill, K.; Bromberg, S. *Molecular driving forces: statistical thermodynamics in biology, chemistry, physics, and nanoscience*; Garland Science, 2010.
(82) Shell, M. S. *Thermodynamics and statistical mechanics: an integrated approach*; Cambridge University Press, 2015.
(83) Sung, W. *Statistical Physics for Biological Matter*; Springer, 2018.
(84) Phillips, R.; Kondev, J.; Theriot, J.; Garcia, H. *Physical Biology of the Cell*; Garland Science (Taylor & Francis Group): London and New York, 2013.
(85) Mulero, Á. *Theory and simulation of hard-sphere fluids and related systems*; Springer, 2008.
(86) De Gennes, P.-G.; Prost, J. *The physics of liquid crystals*; Oxford University Press, 1993.
(87) Berg, J. C. *An introduction to interfaces & colloids: the bridge to nanoscience*; World Scientific, 2010.
(88) Dittmore, A.; McIntosh, D. B.; Halliday, S.; Saleh, O. A. Single-molecule elasticity measurements of the onset of excluded volume in poly (ethylene glycol). *Phys. Rev. Lett.* **2011**, *107* (14), No. 148301.
(89) Hsu, H.-P.; Binder, K. Stretching semiflexible polymer chains: Evidence for the importance of excluded volume effects from Monte Carlo simulation. *J. Chem. Phys.* **2012**, *136*, No. 024901.
(90) Dai, L.; Doyle, P. S. Comparisons of a polymer in confinement versus applied force. *Macromolecules* **2013**, *46* (15), 6336−6344.
(91) Pathria, R. K. *Statistical mechanics*; Elsevier, 2016.
(92) Wang, Z.-G. 50th Anniversary Perspective: Polymer Conformation—A Pedagogical Review. *Macromolecules* **2017**, *50* (23), 9073−9114.
(93) Auhl, R.; Everaers, R.; Grest, G. S.; Kremer, K.; Plimpton, S. J. Equilibration of long chain polymer melts in computer simulations. *J. Chem. Phys.* **2003**, *119* (24), 12718−12728.
(94) Murat, M.; Kremer, K. From many monomers to many polymers: Soft ellipsoid model for polymer melts and mixtures. *J. Chem. Phys.* **1998**, *108* (10), 4340−4348.
(95) Fleury, G.; Brochon, C.; Schlatter, G.; Bonnet, G.; Lapp, A.; Hadziioannou, G. Synthesis and characterization of high molecular weight polyrotaxanes: towards the control over a wide range of threaded α-cyclodextrins. *Soft Matter* **2005**, *1* (5), 378−385.

https://doi.org/10.1021/acs.macromol.3c01805
Macromolecules 2024, 57, 1846−1858

(96) Yamada, S.; Sanada, Y.; Tamura, A.; Yui, N.; Sakurai, K. Chain architecture and flexibility of α-cyclodextrin/PEG polyrotaxanes in dilute solutions. *Polym. J.* **2015**, *47* (6), 464−467.
(97) Doi, M. *Introduction to polymer physics*; Oxford University Press, 1996.

https://doi.org/10.1021/acs.macromol.3c01805
Macromolecules 2024, 57, 1846−1858

Supporting Information

Entropy-Induced Localization and Sliding Dynamics of Rings on Polyrotaxane

Yan Wang[†], *Hui Lu*[†,‡], *Xiang-Meng Jia*[§], *An-Chang Shi*[*,ǁ], *Jiajia Zhou*[*,§], *Guojie Zhang*[*,⊥], *Hong Liu*[*,†,#]

[†] Key Laboratory of Theoretical Chemistry of Environment Ministry of Education, School of Environment, South China Normal University, Guangzhou 510006, China;

[‡] Xuzhou No.35 Middle School, Xuzhou 221000, China;

[§] South China Advanced Institute for Soft Matter Science and Technology, School of Emergent Soft Matter, South China University of Technology, Guangzhou 510640, China;

[ǁ] Department of Physics & Astronomy, McMaster University, Hamilton, Ontario, Canada;

[⊥] School of Chemistry and Chemical Engineering, Guangzhou University, Guangzhou 510006, China;

[#] Guangdong Provincial Key Laboratory of Chemical Pollution and Environmental Safety, South China Normal University, Guangzhou 510006, China.

1. The schematics of the geometric relationship between the ring beads and the coil strand beads

Imagine that the ring is exactly sitting on the *i*-th bead of coil, as schematically shown in **Figure S1**. For simplicity, we still use the scheme applied in **Figure 4b** and we imagine that the ring plane is on the *x*-*y* plane. The limited bending condition for the coil segment is that, the (*i*+1)-th bead closely touches the ring bead (i.e., the bead labeled as *k* in the figure) which is exactly below it. In this condition, we may obtain the largest value of θ_0. Thus, the three beads *i*, *i*+1 and *k* form a triangle. Given the fact that all sizes of beads are set as σ, the three side lengths should be: $d(i{\sim}i+1) \approx \sigma$ (equilibrium bond length as 0.97σ), $d(k{\sim}i+1) = \sigma$ (since they are touched with each other) and $d(i{\sim}k) = 1.24\sigma$. For $d(i{\sim}k)$, we can first evaluate the diameter of the hollow cavity of ring (involving 8 beads) as $d_0 = 8l_0/\pi = 2.47\sigma$ with $l_0 = 0.97\sigma$ as the bond length. Thus $d(i{\sim}k)$ is exactly half of d_0, thus $d(i{\sim}k) = 1.24\sigma$. Therefore, we can easily calculate the angle $\angle(i+1, i, k) = 52°$. Thus, the angle $\theta_0 = 90° - \angle(i+1, i, k) = 38°$. Practically, we use a quite approximate parameter, i.e., $\theta_0 = 39.5°$ to make the fitting and obtain the result in **Figure 4c**.

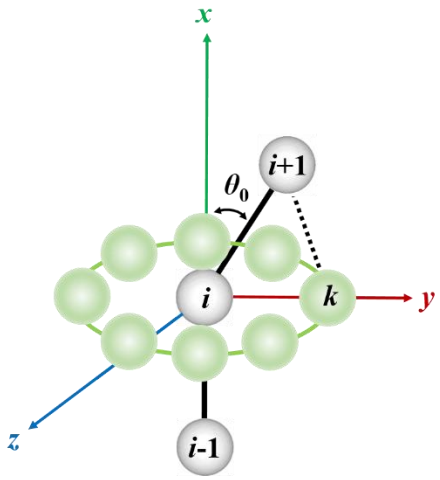

Figure S1. The schematics of the geometric relationship between the ring beads and the coil strand beads. The gray beads represent the three consecutive chain segments *i*-1, *i* and *i*+1 on the coil

strand of PR which are referred from **Figure 4b** of the paper. The connected 8 green beads represent the threaded ring which is exactly sitting the position centered with the *i*-th bead of coil.

2. The impact of polymer thickness on Δ*E*

A new model, i.e., the "rod-normal-coil-slim" model, has been designed to investigate the impact of polymer thickness on ΔE. In this model, the thickness variation between different segments is taken into consideration. The rod segments and rings are composed of beads with a diameter of 1.0σ, which is used to mimic thick polymers, while the beads constituting the coil segments have a diameter set as 0.5σ, which is used to mimic thin or slim polymers. In the original model in the manuscript, the ratio of the thickness for the two segments was set $R_{\mathrm{rod}} : R_{\mathrm{coil}} = 1: 1$, while the ratio for the new model is $R_{\mathrm{rod}} : R_{\mathrm{coil}} = 2: 1$. We employ this approach to achieve distinct thicknesses for rod and coil segments. The following parameter combinations were used (listed in **Table S1**) to simulate models with different thicknesses and calculate the corresponding Δ*E*. We compared the Δ*E* results obtained from models considering varying polymer chain thickness with the previously unconsidered polymer chain thickness model system. The comparison results are illustrated in **Figure S2**. As shown in **Figure S2**, it can be observed that the $R_{rod} : R_{coil} = 2{:}1$ model and the $R_{rod} : R_{coil} = 1{:}1$ model yield similar results. Thus our main conclusion in the manuscript is still valid, i.e., Δ*E* is basically independent on α and N as long as μ and ρ_{ring} are the same.

Table S1. The parameter combinations used for the simulation of the $R_{\mathrm{rod}} : R_{\mathrm{coil}} = 2: 1$ model (with $N = 480, 600$).

μ	α	ρ_{ring}
0.2	0.25	0.05

0.4	0.25	0.05
0.6	3.0	0.05
0.8	3.0	0.05

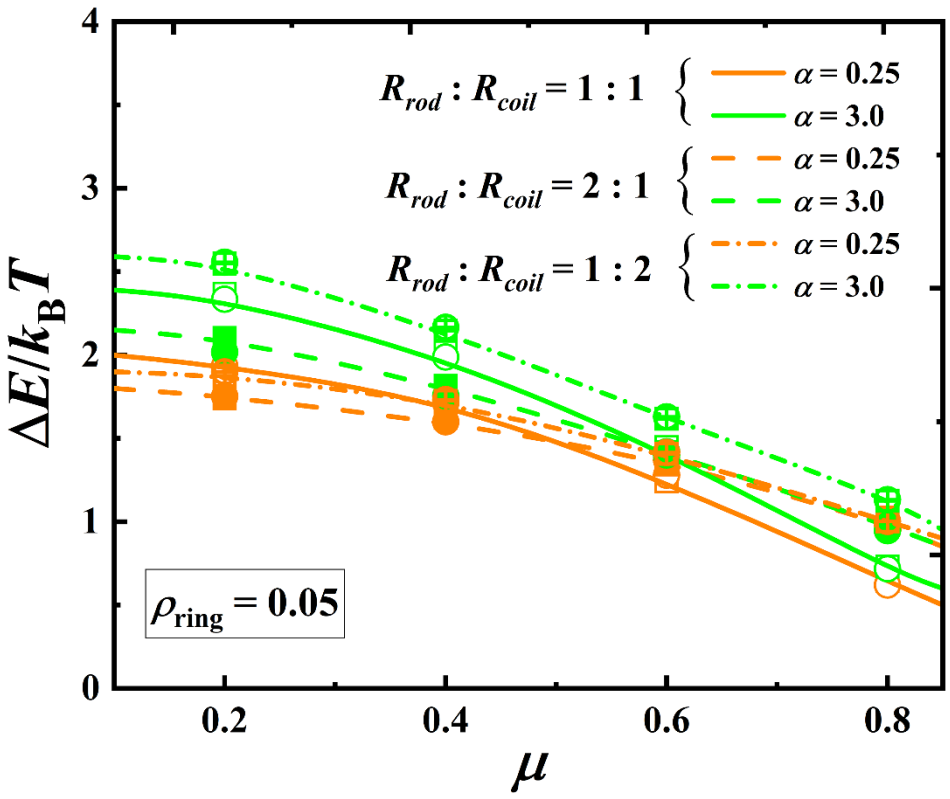

Figure S2. The dependence of ΔE on the characteristic parameter μ in the systems with ρ_{ring} =0.05 and different α in the "rod-normal-coil-slim" model. The different symbols represent models with various N. The square and circle symbols represent N=480 and 600, respectively. The hollow square and circle symbols represent R_{rod} : R_{coil} = 1: 1 models, the solid square and circle symbols represent R_{rod} : R_{coil} = 2: 1 models, while the hollow square and circle with a cross in the center symbols represent R_{rod} : R_{coil} = 1: 2 models. The solid, dashed and short dash dot lines are shown to guide the eye for each group.

3. Hopping dynamics of rings with varying the length of coil strand

To better understand the impact of coil segment length on the ring hopping dynamics, we design a series of models. In these models, the rod length N_r is set to 60. The number of rings is set to 100. The R_{ee} values for the coil segment was set to several fixed values as listed in **Table S2**. By adjusting the coil length N_f values, a series of models were constructed. The specific parameter details are listed in **Table S2**.

Table S2. The parameters for the models of different coil lengths.

N_f	N	α	μ	R_{ee}	ρ_{ring}
20	140	6.00	0.54	10.0	0.71
40	160	3.00	0.53	20.0	0.63
80	200	1.50	0.78	60.0	0.50
160	280	0.75	0.39	60.0	0.36
240	400	0.50	0.40	92.73	0.25
320	440	0.38	0.19	60.0	0.23
400	560	0.30	0.16	60.0	0.18

Based on the systems in Table S2, the hopping dynamics are investigated. As shown in **Figure S3** (a) and (b), the results of the ring hopping dynamics obtained by varying the coil length are generally consistent with those presented in **Figure 8** of the main text. When $\rho_{ring} < 0.5$, the mean count of hopping events significantly increases with the growth of ρ_{ring}. Conversely, when $\rho_{ring} >$

0.5, further increasing ρ_{ring} results in a decrease in the mean count of hopping events. Thus the main principle is still valid for various lengths of the coil strand.

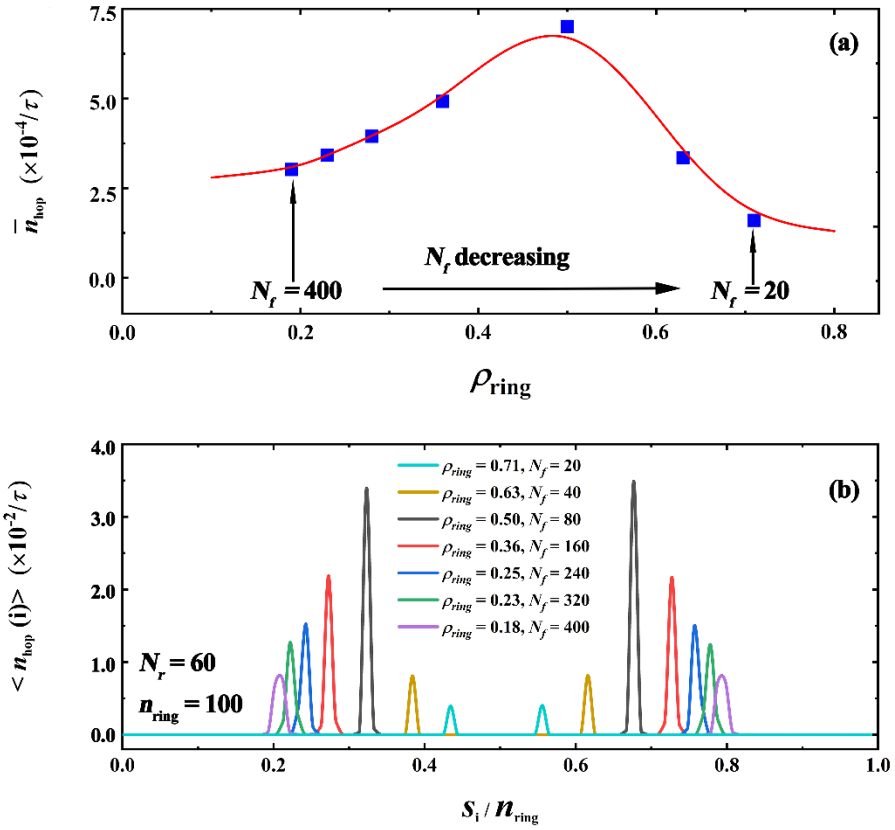

Figure S3. (a) The dependence of mean count of hopping events in unit time of rings $\bar{n}_{\text{hop}}$ on the ring coverage density ρ_{ring} in the multiple-ring-threaded PR system. Each blue scatter represents multiple-ring-threaded PR system with different coil length N_f. The red curve is for guiding the line. (b) The distribution of hopping event counts in unit time $\langle n_{\text{hop}}(\text{i}) \rangle$ of rings on the PR backbone for the systems in Subfigure (a) with different ρ_{ring} and coil chain length N_f. Here n_{ring} is the total number of rings, while S_{i} denotes the index of the i-th ring.

4. The parameters used for simulated models in the manuscript

The parameters used for simulated models for **Figure 2**, **Figure 4(a)**, **Figure 4(c)**, **Figure 8** and **Figure 9** are shown in the following tables.

Table S3. The parameter combinations with N=480, 600, and 720 used for the simulation of **Figure 2** in the manuscript.

Subfigure (a):

$N = 480$

α	μ	ρ_{ring}	N	N_r	N_f	n_{ring}
0.25	0.3	0.2	480	48	384	96
	0.3	0.5	480	48	384	240
	0.7	0.2	480	48	384	96
	0.7	0.5	480	48	384	240
1.0	0.3	0.2	480	120	240	96
	0.3	0.5	480	120	240	240
	0.7	0.2	480	120	240	96
	0.7	0.5	480	120	240	240
2.0	0.3	0.2	480	160	160	96

	0.3	0.5	480	160	160	240
	0.7	0.2	480	160	160	96
	0.7	0.5	480	160	160	240
3.0	0.3	0.2	480	180	120	96
	0.3	0.5	480	180	120	240
	0.7	0.2	480	180	120	96
	0.7	0.5	480	180	120	240

$N = 600$

α	μ	ρ_{ring}	N	N_{r}	N_{f}	n_{ring}
0.25	0.3	0.2	600	60	480	120
	0.3	0.5	600	60	480	300
	0.7	0.2	600	60	480	120
	0.7	0.5	600	60	480	300
1.0	0.3	0.2	600	150	300	120
	0.3	0.5	600	150	300	300

	0.7	0.2	600	150	300	120
	0.7	0.5	600	150	300	300
2.0	0.3	0.2	600	200	200	120
	0.3	0.5	600	200	200	300
	0.7	0.2	600	200	200	120
	0.7	0.5	600	200	200	300
3.0	0.3	0.2	600	225	150	120
	0.3	0.5	600	225	150	300
	0.7	0.2	600	225	150	120
	0.7	0.5	600	225	150	300

$N = 720$

α	μ	ρ_{ring}	N	N_{r}	N_{f}	n_{ring}
0.25	0.3	0.2	720	72	576	144
	0.3	0.5	720	72	576	360
	0.7	0.2	720	72	576	144

	0.7	0.5	720	72	576	360
1.0	0.3	0.2	720	180	360	144
	0.3	0.5	720	180	360	360
	0.7	0.2	720	180	360	144
	0.7	0.5	720	180	360	360
2.0	0.3	0.2	720	240	240	144
	0.3	0.5	720	240	240	360
	0.7	0.2	720	240	240	144
	0.7	0.5	720	240	240	360
3.0	0.3	0.2	720	270	180	144
	0.3	0.5	720	270	180	360
	0.7	0.2	720	270	180	144
	0.7	0.5	720	270	180	360

Subfigure (b):

$N = 480$

μ	α	ρ_{ring}	N	N_{r}	N_{f}	n_{ring}
0.2	0.25	0.05	480	48	384	24
	0.25	0.4	480	48	384	192
	3.0	0.05	480	180	120	24
	3.0	0.4	480	180	120	192
0.4	0.25	0.05	480	48	384	24
	0.25	0.4	480	48	384	192
	3.0	0.05	480	180	120	24
	3.0	0.4	480	180	120	192
0.6	0.25	0.05	480	48	384	24
	0.25	0.4	480	48	384	192
	3.0	0.05	480	180	120	24
	3.0	0.4	480	180	120	192
0.8	0.25	0.05	480	48	384	24
	0.25	0.4	480	48	384	192
	3.0	0.05	480	180	120	24

	3.0	0.4	480	180	120	192

$N = 600$

μ	α	ρ_{ring}	N	N_r	N_f	n_{ring}
0.2	0.25	0.05	600	60	480	30
	0.25	0.4	600	60	480	240
	3.0	0.05	600	225	150	30
	3.0	0.4	600	225	150	240
0.4	0.25	0.05	600	60	480	30
	0.25	0.4	600	60	480	240
	3.0	0.05	600	225	150	30
	3.0	0.4	600	225	150	240
0.6	0.25	0.05	600	60	480	30
	0.25	0.4	600	60	480	240
	3.0	0.05	600	225	150	30
	3.0	0.4	600	225	150	240

0.8	0.25	0.05	600	60	480	30
	0.25	0.4	600	60	480	240
	3.0	0.05	600	225	150	30
	3.0	0.4	600	225	150	240

$N = 720$

μ	α	ρ_{ring}	N	N_{r}	N_{f}	n_{ring}
0.2	0.25	0.05	720	72	576	36
	0.25	0.4	720	72	576	288
	3.0	0.05	720	270	180	36
	3.0	0.4	720	270	180	288
0.4	0.25	0.05	720	72	576	36
	0.25	0.4	720	72	576	288
	3.0	0.05	720	270	180	36
	3.0	0.4	720	270	180	288
0.6	0.25	0.05	720	72	576	36

	0.25	0.4	720	72	576	288
	3.0	0.05	720	270	180	36
	3.0	0.4	720	270	180	288
0.8	0.25	0.05	720	72	576	36
	0.25	0.4	720	72	576	288
	3.0	0.05	720	270	180	36
	3.0	0.4	720	270	180	288

Subfigure (c):

$N = 480$

ρ_{ring}	μ	α	N	N_r	N_f	n_{ring}
0.05	0.2	0.25	480	48	384	24
	0.2	3.0	480	180	120	24
	0.6	0.25	480	48	384	24
	0.6	3.0	480	180	120	24
0.2	0.2	0.25	480	48	384	96

	0.2	3.0	480	180	120	96
	0.6	0.25	480	48	384	96
	0.6	3.0	480	180	120	96
0.4	0.2	0.25	480	48	384	192
	0.2	3.0	480	180	120	192
	0.6	0.25	480	48	384	192
	0.6	3.0	480	180	120	192
0.6	0.2	0.25	480	48	384	288
	0.2	3.0	480	180	120	288
	0.6	0.25	480	48	384	288
	0.6	3.0	480	180	120	288

$N = 600$

ρ_{ring}	μ	α	N	N_r	N_f	n_{ring}
0.05	0.2	0.25	600	60	480	30
	0.2	3.0	600	225	150	30

	0.6	0.25	600	60	480	30
	0.6	3.0	600	225	150	30
0.2	0.2	0.25	600	60	480	120
	0.2	3.0	600	225	150	120
	0.6	0.25	600	60	480	120
	0.6	3.0	600	225	150	120
0.4	0.2	0.25	600	60	480	240
	0.2	3.0	600	225	150	240
	0.6	0.25	600	60	480	240
	0.6	3.0	600	225	150	240
0.6	0.2	0.25	600	60	480	360
	0.2	3.0	600	225	150	360
	0.6	0.25	600	60	480	360
	0.6	3.0	600	225	150	360

$N = 720$

ρ_{ring}	μ	α	N	N_r	N_f	n_{ring}
0.05	0.2	0.25	720	72	576	36
	0.2	3.0	720	270	180	36
	0.6	0.25	720	72	576	36
	0.6	3.0	720	270	180	36
0.2	0.2	0.25	720	72	576	144
	0.2	3.0	720	270	180	144
	0.6	0.25	720	72	576	144
	0.6	3.0	720	270	180	144
0.4	0.2	0.25	720	72	576	288
	0.2	3.0	720	270	180	288
	0.6	0.25	720	72	576	288
	0.6	3.0	720	270	180	288
0.6	0.2	0.25	720	72	576	432
	0.2	3.0	720	270	180	432
	0.6	0.25	720	72	576	432

	0.6	3.0	720	270	180	432

Table S4. The parameters for the simulated models used in Figure 4(a) and Figure 4(c).

μ	R_{ee}	N_r	N_f	α
0.2	7.566	5	40	0.25
	3.686	10	20	1.0
	3.686	20	20	2.0
	3.686	40	20	4.0
	3.686	80	20	8.0
	3.686	120	20	12.0
0.3	11.349	5	40	0.25
	8.439	15	30	1.0
	8.439	30	30	2.0
	8.439	60	30	4.0
	8.439	120	30	8.0
	8.439	180	30	12.0

0.4	15.132	5	40	0.25
	15.132	20	40	1.0
	15.132	40	40	2.0
	15.132	80	40	4.0
	15.132	160	40	8.0
	15.132	240	40	12.0
0.5	18.915	5	40	0.25
	23.765	25	50	1.0
	23.765	50	50	2.0
	23.765	100	50	4.0
	23.765	200	50	8.0
	23.765	300	50	12.0
0.6	36.666	5	40	0.25
	34.338	30	60	1.0
	34.338	60	60	2.0
	34.338	120	60	4.0

34.338	240	60	8.0
34.338	360	60	12.0

Table S5. The parameters for the simulated models used in **Figure 8**.

N_f	N_r	N	α	μ	n_{ring}	ρ_{ring}
80	20	120	0.5	0.4	100	0.83
120	30	180	0.5	0.4	100	0.56
100	25	150	0.5	0.4	75	0.50
100	25	150	0.5	0.4	60	0.40
200	50	300	0.5	0.4	100	0.33
240	60	360	0.5	0.4	100	0.28
100	25	150	0.5	0.4	30	0.20

Table S6. The parameters for the simulated models used in **Figure 9**.

N_f	N_r	N	α	μ	R_{ee}	n_{ring}	ρ_{ring}
60	60	180	2.0	0.2	11.45	36	0.20

60	60	180	2.0	0.3	17.17	36	0.20
60	60	180	2.0	0.4	22.90	36	0.20
60	60	180	2.0	0.5	28.62	36	0.20
60	60	180	2.0	0.6	34.34	36	0.20
60	60	180	2.0	0.7	40.061	36	0.20
60	60	180	2.0	0.8	45.78	36	0.20